

Space-time simulation of precipitation based on weather pattern sub-sampling and meta-Gaussian model

Pradeebane Vaittinada Ayar, Juliette Blanchet, Emmanuel Paquet, David Penot

▶ **To cite this version:**

Pradeebane Vaittinada Ayar, Juliette Blanchet, Emmanuel Paquet, David Penot. Space-time simulation of precipitation based on weather pattern sub-sampling and meta-Gaussian model. Journal of Hydrology, 2020, 581, pp.124451. 10.1016/j.jhydrol.2019.124451 . hal-03087662

HAL Id: hal-03087662
https://hal.science/hal-03087662

Submitted on 21 Dec 2021

HAL is a multi-disciplinary open access archive for the deposit and dissemination of scientific research documents, whether they are published or not. The documents may come from teaching and research institutions in France or abroad, or from public or private research centers.

L'archive ouverte pluridisciplinaire **HAL**, est destinée au dépôt et à la diffusion de documents scientifiques de niveau recherche, publiés ou non, émanant des établissements d'enseignement et de recherche français ou étrangers, des laboratoires publics ou privés.



Distributed under a Creative Commons Attribution - NonCommercial 4.0 International License

Version of Record: https://www.sciencedirect.com/science/article/pii/S0022169419311862
Manuscript_7fba457bff4443cb05ce7369659c27cf

Space-time simulation of precipitation based on weather pattern sub-sampling and meta-Gaussian model.

Pradeebane Vaittinada Ayar[a,*], Juliette Blanchet[a], Emmanuel Paquet[b], David Penot[b]

[a] *Univ. Grenoble Alpes, CNRS, IGE, F-38000 Grenoble, France*
[b] *EDF – DTG, 21 Avenue de l'Europe, BP 41, 38040 Grenoble Cedex 9, France*

Abstract

Simulation methods for design flood estimations in dam safety studies require fine scale precipitation data to provide quality input for hydrological models, especially for extrapolation to extreme events. This leads to use statistical models such as stochastic weather generators. The aim here is to develop a stochastic model adaptable on mountainous catchments in France and accounting for spatial and temporal dependencies in daily precipitation fields. To achieve this goal, the framework of spatial random processes is adopted here.

The novelty of the model developed in this study resides in the combination of an autoregessive meta-Gaussian process accounting for the spatio-temporal dependencies and weather pattern sub-sampling discriminating the different rainfall intensity classes. The model is tested from rain gauges in the Ardèche catchment located in South of France. The model estimation is performed in four steps, dealing respectively with: (i) the at-site marginal distribution, (ii) the mapping of the marginal distribution parameters at the target resolution, (iii) the at-site temporal correlation and (iv) the spatial covariance function.

The model simulations are evaluated in terms of marginal distribution, inter-site dependence and areal rainfall properties and compared to the observations at calibration stations and also on a set of independent validation stations. Regarding all these aspects, the model shows good abilities to reproduce the observed

*Corresponding author
Email address: pradeebane@laposte.net (Pradeebane Vaittinada Ayar)

© 2019 published by Elsevier. This manuscript is made available under the CC BY NC user license
https://creativecommons.org/licenses/by-nc/4.0/

statistics and presents really small discrepancies compared to the stations data. The sub-sampling is particularly efficient to reproduce the seasonal variations and the marginal mapping procedure induces very small differences in terms of daily rain amounts and daily occurrence probabilities.

Keywords:

Latent gaussian process, Weather Pattern, Rainfield generation

2010 MSC: 00-01, 99-00

---

1. Intoduction

Stochastic methods embedding rainfall-runoff simulation are now commonly used for extreme flood estimation, like the SCHADEX method (Paquet et al., 2013), or the SEFM method (Schaefer and Barker, 2002). Lumped hydrological models can be considered in this context, but a more detailed representation of hydrological processes varying in space, or the need of information within the catchment (and not only at the outlet) require the implementation of distributed rainfall-runoff models. In a stochastic process, being continuous or event-based, such models have to be fed by either a multi-site or a rain-field simulation model. The presented model is dedicated to this context, and more precisely to future applications to dam safety studies.

A large variety of models has been developed to answer the need for spatially coherent rainfall simulation. The main difficulty lies in the intermittent nature of precipitation. Thus, the modelling has to deal with two different processes: the occurrence and the intensity. In hydro-climatology, the panel of stochastic weather generators is extremely wide. Each model reproduces the different spatio-temporal properties of precipitation with its own benefits or drawbacks. Models available in the literature can be divided into two families.

- *Random resampling models.* The principle is to rearrange past observations in order to get new time series. These models do not allow to generate unobserved values, and in particular the extreme ones needed in dam safety analyses.

- *Random generator models.* The principle is to fit distributions from which new times series can be generated. These models can generate unobserved values. In this family, mainly two types of model are available:
  - *Multi-site models.* These models are able to generate rainfall only at the stations on which they have been calibrated. This type of model allows to prescribe the observed spatial dependence for each pair of stations.
  - *Random fields models.* These models are able to generate rainfall on a regular grid of a chosen resolution whether or not there is stations in the grid cells, thanks to a covariance function. However, the rain gauge network has to be dense enough to be able to learn the spatial properties of the rain field.

These models are often used in two simulation context:

1. *Observation-based models:*in this family the models only aim at mimicking the statistical properties of the observations. Among them, there are resampling models using for instance $k-$nearest neighbours algorithm (*knn*, *e.g.* Buishand and Brandsma, 2001; Leander and Buishand, 2009). There are also rainfall generators mainly based on an underlying Gaussian process. These models rely on the transformation of the non-Gaussian marginals into Gaussian ones. They are hereafter referred to as meta-Gaussian. Many multi-site or rain-field simulators are based on this principle. For the rain-field simulators, a covariance function has to be estimated additionally.

   In order to cope with rain intermittency and rain intensity two strategies are possible. One consists in using a single underlying Gaussian process which is on the one hand truncated for the rain occurrence, and on the other hand transformed for rain intensity. Bàrdossy and Pegram (2009), and Rasmussen (2013) have developed a multi-site model based on a multivariate latent autoregressive Gaussian process to model rain occurrence

and rain intensity processes at the same time. Similarly, Sparks et al. (2018) have recently provided a multi-site multivariate model for minimum, maximum temperature and precipitation based on a single latent autoregressive Gaussian process. Many rain-field simulation strategies over an entire region are also possible from at-site estimated rain distribution and covariance function. A variety of meta-Gaussian models with a single field for occurrence and intensity can be found in the literature (*e.g.,* Sigrist et al., 2012; Baxevani and Lennartsson, 2015). For instance, simulations can be performed over a regular grid by considering the same at-site distribution for all gauges with unconditional simulations (Guillot, 1999; Guillot and Lebel, 1999) or conditional ones (Vischel et al., 2009). A kriging can be done over marginal distribution parameters estimated at each station in order to get spatially varying marginals at a desired target resolution. These marginals are combined with a meta-Gaussian rain-field simulator to generate daily rain fields (Bennett et al., 2018). Another way is to use two distinct processes to model the occurrence and the intensity. Multi-site models based on that principle are available (Wilks, 1998; Evin et al., 2018). Based on the same idea, rain fields are also simulated by combining marginal parameters kriging with two distinct processes (*e.g.,* Kleiber et al., 2012; Verdin et al., 2015).

Based on meta-Gaussian process, models for high spatio-temporal resolution accounting for the advection of the rain process have also been developed (Leblois and Creutin, 2013; Paschalis et al., 2013; Peleg et al., 2017; Benoit et al., 2018a). Event based modelling can also be adopted instead of using a fixed time scale (daily for instance *e.g.,* Onof et al., 2000; Leonard et al., 2008; Burton et al., 2010).

2. *Exogenous variables-constrained models:* in this family the models explicitly use exogenous variables as covariates (or predictors): these are the so-called downscaling models (cf. Vaittinada Ayar et al., 2016; Gutiérrez et al., 2018, for intercomparisons). The principle is to statistically link observations with synoptic information at coarse resolution extracted for

instance, from climate models in order to simulate precipitation. Part of the climate non-stationarity carried by the synoptic variable is, by construction, taken into account in the stochastic model. These models can be used to reconstruct past events, perform short-term predictions or climate projections from future climate simulations of global circulation model. Resampling models can be based on atmospheric analog (Yiou, 2014) or on non-parametric geostatistical methods (Jha et al., 2015). Many generators are based on Generalised Linear Models (GLM) to link the predictors with the observations. Many examples of meta-Gaussian multi-sites models have been also proposed (cf. Wilks, 2010, 2012, for a review). For instance, Chandler (2002) has proposed a rain-field simulator with two distinct processes for rain occurrence and intensity but only applied in a multi-site context. Two other studies conducted by Yang et al. (2005) et Ambrosino et al. (2014) have applied a modified version of this model. Estimated from a gridded dataset, Serinaldi and Kilsby (2014) have used a single latent Gaussian process to simulate rain field at the observations resolution.

Hybrid models:. many models that can be described as hybrid. This family gathers the models using components from both aforementioned families. These models combine resampling, multi-sites or random fields approaches and a synoptic information through a discrete variable. Atmospheric circulation patterns are summarised and discretised into different classes. If these classes are established directly from the precipitation or from synoptic variables these are respectively referred to as Precipitation Types (PTs) or Weather Types (WTs). Precipitations are generated conditionally to this discrete variable.

It is possible to perform resampling conditionally to WTs or PTs, *i.e.* the resampling is only performed within a class. For instance, a Hidden Markov Model (HMM) used to generate PTs sequence (Steinschneider and Brown, 2013) or a WTs classification (Caraway et al., 2014) can be combined with a *knn* method. A simple multi-site modelling consists in considering the stations as spatially

and temporally independent given a WT which can be modelled by a HMM (Zucchini and Guttorp, 1991; Hughes and Guttorp, 1994; Bellone et al., 2000), or defined explicitly (Vrac et al., 2007). Bellone et al. (2000) and Vrac et al. (2007) estimate the transition probabilities from one WT to another as functions of synoptic variables (by GLM). Thompson et al. (2007) consider a multi-site daily rainfall generator in which rainfall spatial dependence conditionally to station-specific PTs. Ailliot et al. (2009) modify this model by first considering regional PTs and second adopting a rain-field generator instead of a multi-site generator. A wide range of statistical models conditioned by WTs are suggested in the literature (cf. Wilks, 2010, 2012; Ailliot et al., 2015, for reviews). Based on the same idea, event-based models accounting for the advection and for sub-daily data have also been developed (*e.g.* Peleg and Morin, 2014).

Using PTs or WTs are both valid options to define rain intensity classes. PTs define rather catchment-specific classes since they are defined from observations. On the contrary, WTs are defined over larger areas being defined by synoptic variables and are not specific to one catchment. WTs defined over France mountainous regions have been proved to be efficient for rainfall distribution modelling over France (Garavaglia et al., 2010, 2011; Evin et al., 2016; Blanchet et al., 2019). The present paper investigates the added-value of these WTs in the context of rainfall spatial modelling over mountainous regions in France.

In this study, an hybrid model of daily rain-field is developed. The model further presented is closely related to the model of Ailliot et al. (2009). Their approach lies on the combination of a HMM for the PTs generation and a rain-field simulator which covariance function is estimated conditionally to a PTs. Our model departs from the latter on three points:

1. PTs are replaced by WTs which are not specific to a given catchment. WTs sequence is not modelled, instead a long observed sequence is played as many times as needed (*e.g.* if 1000-years long rainfall sequence is needed, the observed WT sequence of 40 years is repeated 25 times),

2. Temporal dependence is not implicitly ensured by the sequence of WTs but is explicitly modelled conditionally to transitions from a WT to another,
3. The model is not only used in a multi-site contexte: simulations are not only generated at calibration stations. This model allows to generate rainfall at any location of the catchment or to upscale at a target spatial resolution to generate fields (1km^2 for instance).

The novelty lies in the development of an hybrid random rain-field simulator that is fed by daily rain-gauge data only and in which all the model components, namely the marginal distributions and the spatio-temporal dependence structure, are conditioned by synoptic WTs. This has to our knowledge never been proposed before.

The aim is to get a model adaptable to different mountainous catchments covering several thousands square kilometre. A daily time-step is relevant in these cases, as well for the dynamic of the hydrological processes to be modelled, as for the availability of the rainfall data. A special attention is paid to the ability of the model to simulate the high quantiles, and to the good representation of the day to day correlation of wet sequences, in order to model coherent hydrographs. Section 2 presents the study area and the data. Section 3 describes the model. The simulations are evaluated in Section 4 and Section 5 gives the conclusions, discusses the results and presents some perspectives of the proposed work.

2. Study area and data

To assess the model ability to meet the previously stated objectives an application to the Ardèche catchment (2260 km^2) located in the south-east of France (cf. Fig. 1) is made. Indeed, despite its size, this catchment presents important orographic and climatic disparities. This region partly includes the south-eastern slope of the Massif Central where the highest summits are located (about 1700 m.a.s.l.), and bordered by the Rhône valley (down to 40 m.a.s.l.) in the East. This region is prone to extreme precipitations causing intense floods

(Delrieu et al., 2005; Nuissier et al., 2008). These events are mainly triggered by the advection of humid air mass of the lower layer of the atmosphere flown from the Mediterranean sea and forming meso-scale convective and quasi-stationary systems. Due to the specific topography, these systems can stay over the same area for several hours and are responsible for heavy rainfall (Nuissier et al., 2008). The HyMeX field campaign (Ducrocq et al., 2014; Drobinski et al., 2014) gives a thorough insight into the large variety of blocking situation generating heavy rainfall systems over the region.

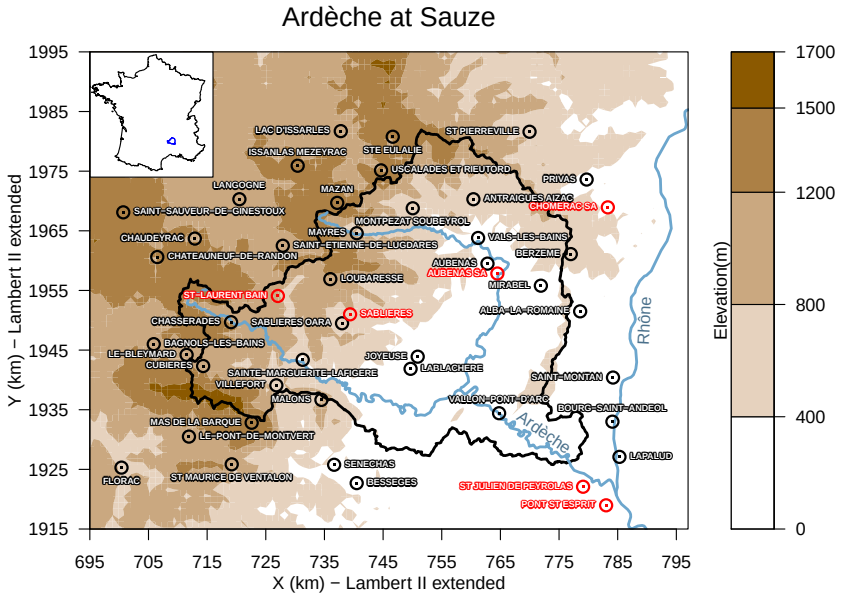


Figure 1: Map of the studied region. Superficie: 2,260 km^2 – 47 Stations – Station elevation: from 47 to 1425 m – Red stations are validation stations.

Data from rain gauge networks operated by Électricité de France and Météo France are used. Forty seven stations are available inside and outside the catchment with 15 to 40 years of daily data between January 1, 1969 and December 31 2008. Figure A.1 (Appendix A) shows the data availability throughout the period for each station.

The proposed stochastic model aims at generating rain fields at a given

resolution to provide rainfall scenarios in order to simulate flood events thanks to a rainfall-runoff model. This study only describes and evaluates the rainfall generator model. Among the 47 stations, $N = 41$ stations (black stations in Figure 1) are used to calibrate the model and to evaluate it from simulations performed at these stations. In order to evaluate the potential errors or biases that will be faced when simulating fields, six leave-out (or validation) stations are kept (red stations in Figure 1). The performance of the model is evaluated at these stations in order to enlighten the potential errors in non-monitored areas.

In the next sections, the simulator structure and its application over the Ardèche catchment are presented. The modelling choices are driven by the will to combine WTs with a Gaussian process and are not specific to the Ardèche catchment. In order to illustrate the adaptability of the model framework to different catchment, the model is also tested over the Durance catchment. This question is discussed in Section 4.4 and all the results for this catchment are available in the supplementary material.

3. Spatial simulator

In this section, the different components of the model are described. The simulator is based on a single meta-Gaussian process to model both rain occurrence and intensity. This approach is privileged in order to reduce the number of estimated parameters and simulated Gaussian fields (especially in the case of high resolution random fields) and to maintain the spatio-temporal coherence between rain occurrence and intensity.

Let $\mathbf{x} = (x_1, \cdots, x_N)$ be the vector of length N of station locations. According to Guillot (1999), the vector of precipitation $Y(\mathbf{x})$ at stations $\mathbf{x}$ is linked to the latent Gaussian vector $Z(\mathbf{x})$ by the following relationship:

$$Y(\mathbf{x}) = \begin{cases} \Psi(Z(\mathbf{x})), & \text{if } Z(\mathbf{x}) > C(\mathbf{x}) \\ 0, & \text{if } Z(\mathbf{x}) \leq C(\mathbf{x}) \end{cases} \tag{1}$$

where Ψ is a monotonic non-decreasing function (further described in Equation 2 and 3) from which rain intensity is retrieved by transforming Z values above C. C is a threshold which prescribes the rain intermittency.

Given the fact that the rain generating processes can have different nature (*e.g.* stratiform or convective) or evolve seasonally (heavier rain intensity in Autumn are observed over the region), the seasonal and WT-based sub-sampling proposed by Garavaglia et al. (2010) is adopted. Indeed, a split in $S = 2$ seasons is set (with a low-risk season LO from December to August and a high-risk season HI from September to November). However, instead of the eight WTs identified at the Western European scale by Garavaglia et al. (2010), those are grouped into $K = 3$ Groups of weather Types (GT) based on the correlogram characterising the spatial correlation of the rain fields (the same GT as defined in Blanchet et al., 2019). GTs frequencies between 1969-2008 are given in Table 1. GT1 mainly regroups Mediterranean circulations bringing the heavy rain events over the study region. GT2 rather regroups oceanic (Atlantic) circulations based rainfall and GT3 gathers anticyclonic days (with really sparse or no rainfall). The rainfall intensity, correlation range decreases from GT1 to GT3 (cf. Table 1 and Blanchet et al., 2019). The distinction between convective and stratiform rainfall is mainly taken into account by the seasonal/GT sub-sampling. In the following, each day $t = 1, \ldots, T$ is thus associated to a sub-set $j \in [1, \cdots, S \times K = 6]$.

Table 1: Annual and seasonal percentage of the three GTs for the period 1969-2008. The WT defined by Garavaglia et al. (2010) composing each GT are given into brackets. LO season extends from December to August, HI season from September to November. Into square bracket are given the minimum median and maximum of the annual and seasonal averages of daily non-zero rainfall of the 47 stations.

	Year	LO	HI
GT1 (3-4-7)	28% [8.1 15.0 30.7]	27% [7.6 12.8 26.4]	31% [9.3 21.4 42.2]
GT2 (1-2-6)	35% [4.0 6.9 10.2]	36% [3.9 6.5 9.7]	33% [4.3 8.6 12.7]
GT3 (5-8)	37% [2.5 4.2 8.3]	37% [2.5 4.3 7.6]	35% [1.6 3.8 10.9]

In the following sections, the at site marginal model and the parameters mapping are presented in Section 3.1, the spatio-temporal dependence in Section 3.2 and all the parameters estimations are presented in Section 3.3. The model steps are summarised in Figure 2, and the notations are reminded in Table 2.

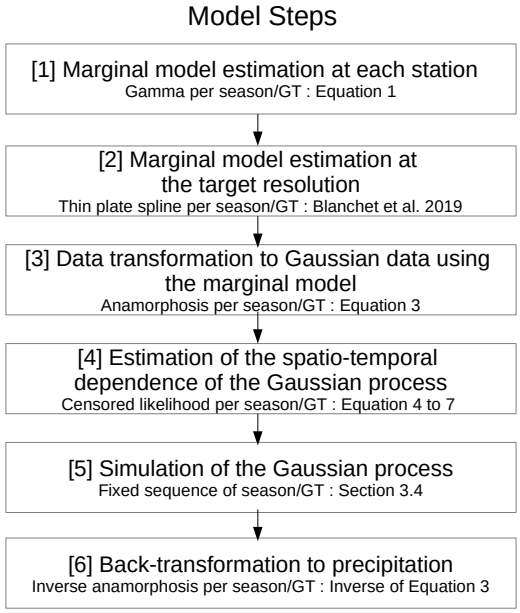


Figure 2: Schematic summary of the full estimation and simulation process.

Table 2: Model notations associated with their respective each steps in Figure 2.

Step	Notations	Definition
[1]	$\hat{p}_j^0(x)$	Dry day fraction estimated at site x for sub-set j
	$\widehat{H}_{Y_j(x)}$	Rainfall CDF estimated at site x for sub-set j
[2]	$\widetilde{H}_{Y_j(x)}$	Mapped rainfall CDF for sub-set j at any point of the domain
[3]	$Z_t(x)$	Censored Gaussian variable associated with the site x
	$c_j(x)$	Censoring threshold of $Z_t(x)$ at site x for sub-set j
[4]	G_t	Spatio-temporal Gaussian process
	$\rho_j(\tau)$	Anisotropic spatial covariance function for sub-set j
	β_j	Parameters of $\rho_j(\tau)$ for sub-set j
	$\alpha_{k,l}^s$	Temporal lag-1 correlation for season s and the transition from GT k to GT l

3.1. Marginal distribution

One of the model ability is to generate rainfall at any location of the domain or on a regular grid. To this end, marginal distribution parameters have to be mapped based on the rain gauge observations. Given the density of the stations and the daily time scale of study, a 1×1 km^2 interpolation grid is considered. Interpolation is achieved for each sub-set j, in a two-step procedure put in place by Blanchet et al. (2019) and illustrated for the same catchment. The marginal distribution at station x relies on the sub-sampling into seasons and GTs. For a given day in sub-set j, the rainfall CDF is given by

$$P(Y_j(x) \leq y) = H_{Y_j(x)}(y) = p_j^0(x) + (1 - p_j^0(x))F_{Y_j(x)}(y) \tag{2}$$

where $Y_j(x)$ is the random variable of daily (zero and non-zero) rainfall amount for a day in sub-set j at x. $p_j^0(x)$ is the dry day fraction at station x within sub-set j. Following the two-step estimation procedure developed in Blanchet

et al. (2019): first the at-site distribution parameters are estimated, then these parameters are mapped at the wanted resolution. The interpolated values can be interpreted as estimates of the local values at the center of the 1×1 km^2 grid points. In Blanchet et al. (2019), the interpolated values are validated at the stations, as if the latter were all located at the center of the grid points they belong to. Blanchet et al. (2019) conclude that, for this study area, the best marginal model is the mixture of gamma distribution (i.e. $F_{Y_j(x)}$ is a Gamma distribution specific for each sub-set j). Blanchet et al. (2019) also found that over this domain the best mapping model is a bivariate thin plate spline model with drift in smoothed elevation. It is shown in the following that the interpolation is statistically quite robust to depict several rainfall characteristics at the station locations.

3.2. Spatio-temporal model

Since the marginal distribution only describes the rainfall behaviour at a given site, the spatial and temporal dependences have to be modelled. If $Y_t(x)$ were real valued, then

$$Z_t(x) = \Phi^{-1}\left[H_{Y_j(x)}\left[Y_t(x)\right]\right], \tag{3}$$

would be a Gaussian process with marginals $\mathcal{N}(0,1)$ (Φ being the standard Gaussian). However since rainfall amounts are non-negative ($Y_t(x) \geq 0$), $Z_t(x)$ defined above is a censored Gaussian process. It can be written as $Z_t(x) = max(c_j(x), G_t(x))$, where $c_j(x) = \Phi^{-1}(p_j^0(x))$ is the censoring threshold and $G_t(x)$ is a mutivariate Gaussian with margins $\mathcal{N}(0,1)$ and covariance matrix Σ_t. Referring to Equation 1, Ψ is equal to $H^{-1}_{Y_j(x)} \circ \Phi$.

The spatio-temporal dependence among the N stations is modelled by the zero-mean latent multivariate Gaussian variable $G = [g_t(x_i); i = 1, \ldots, N; t = 1, \ldots, T]$ $\sim \mathcal{N}(0, \Omega)$ with Ω the $NT \times NT$ covariance matrix for the N sites and T days. It is assumed to be a multivariate Markov autoregressive process of order 1 (MAR(1)). MAR(1) has been used in several studies to describe spatio-temporal

dependence of rainfall (*e.g.* Rasmussen, 2013; Bennett et al., 2018). Thus, $G_t(\mathbf{x})$ is defined as follows:

$$G_t(\mathbf{x}) = A_{t,t-1}G_{t-1}(\mathbf{x}) + E_t(\mathbf{x}). \tag{4}$$

where $A_{t,t-1}$ is a $N \times N$ matrix of autoregressive parameters and $E_t(\mathbf{x})$ is a Gaussian noise vector of length N. The $E_t(\mathbf{x})$s, $t = 1, \ldots, T$, are independent of each other and $E_t(\mathbf{x})$ is independent of $G_{t'}(\mathbf{x})$ for $t' < t$. This ensures the Markovian property. Then $E_t(\mathbf{x})$ has zero mean and covariance matrix $\Sigma_t - A_{t,t-1}^2\Sigma_{t-1}$. The matrix $A_{t,t-1}$ is assumed to be diagonal (*e.g.* Evin et al., 2018; Bennett et al., 2018). This means that only the spatial covariance and the at-site autocorrelation are explicitly modelled.

3.2.1. Spatial dependence

Rain-field simulation based on Gaussian processes requires to calculate the correlation between every couple of points of a domain. In order to achieve that the covariance matrix Σ_t is represented by a covariance function $\rho_j(\tau)$ for a day t in sub-set season/GT j (τ is the inter-site distance). The powered-exponential correlation function is used here $\rho_j(\tau) = \exp\left(-(\frac{\tau}{\lambda_j})^{\nu_j}\right)$, where $\lambda_j > 0$ is the range parameter and $\nu_j \in]0; 2]$ is the power term.

In the literature, anisotropic covariance functions are commonly used to introduce a preferential dependence axis (*e.g.* Baxevani and Lennartsson, 2015; Blanchet and Creutin, 2017). This can be easily done by using a distance accounting for the directionality such as the Mahalanobis distance: $\tau(x_u, x_v) = \sqrt{(x_u - x_v)^T\Pi^{-1}(x_u - x_v)}$. Π is positive definite matrix (with $\Pi = Id_N$ the identity matrix, it gives the euclidean distance) introducing the anisotropy. Π is usually written as $\Pi^{-1} = M^T M$ and M is parametrised as following:

$$M = \begin{pmatrix} \cos\psi & \sin\psi \\ -b\sin\psi & b\cos\psi \end{pmatrix}$$

with $b > 1$ the elongation coefficient and $\psi \in \left[-\frac{\pi}{2}, \frac{\pi}{2}\right]$ the angle. With this parametrisation, for a given site x all the points with equal covariance with x

form an ellipse centred at x with ψ the angle between the horizontal and the major axis of the ellipse and b the ratio between the major and minor axes.

3.2.2. Temporal dependence

As previously mentioned, only the at-site autocorrelation is modelled here since A is a diagonal matrix. Another approximation is made on matrix $A_{t,t-1}$ by considering the autocorrelation as constant over the region. Thus, $A_{t,t-1}$ is of the form $A_{t,t-1} = a_{t,t-1} Id_N$. This also simplifies the covariance of E_t which becomes $\Sigma_t - a_{t,t-1}^2 \Sigma_{t-1}$. In the following, the $a_{t,t-1}$ only depends on transitions among GTs within a season. This coefficient is assumed to be constant within a season and for each transition from one GT to another (from GT1 to GT1, GT1 to GT2, GT2 to GT1 etc.). For t and $t-1$ in a season s and a couple of GTs (k, l), $a_{k,l}^s$ is defined as the autocorrelation coefficient for the transitions from $j_{t-1} = (s, k)$ to $j_t = (s, l)$. In total 18 coefficients have to be estimated.

3.3. Parameters estimation

3.3.1. Marginal distribution parameters

The probability $p_j^0(x)$ is the dry day fraction at station x in sub-set j. The empirical probability $\hat{p}_j^0(x)$ is considered as a good estimate of $p_j^0(x)$. At each station x and for each sub-set j, the parameters of the gamma distribution modelling positive rainfall are estimated by a probability weighted moments method (PWM, cf. Blanchet et al., 2019, for more details). From the estimated $\widehat{H}_{Y_j(x)}$, the precipitations $y_j(x)$ are transformed into $z_j(x)$ used for the estimation of the covariance function (see Section 3.3.2). The marginal model parameters are mapped by a bivariate thin plate spline estimated by a penalised least square method (for more details see Blanchet et al., 2019). A marginal distribution $\widetilde{H}_{Y_j(x)}$ can now be obtained at each point of the domain for each sub-set j from the mapped parameters. The marginal distribution at the six validation stations are computed according this method.

3.3.2. MAR(1) model parameters

From the estimated marginal distributions $\widehat{H}_{Y_j(x)}$, realisations of $Z_t(x)$ at station x for a day t in sub-set $j = (s,k)$: $z_t(x) = \Phi^{-1}(\widehat{H}_{Y_j(x_i)}(y_t(x_i)))$ are computed. From this, the autoregressive parameters $a^s_{k,l}$ and the covariance function ρ_j of G_t for t in sub-set j are estimated. The authors remind that the latent process $G \sim \mathcal{N}(0,\Omega)$ is not observed but only a censored version Z. The use of a censored likelihood is then required. One can write this likelihood for the Gaussian process G described by the Equation 4, nevertheless it represents a numerical challenge to optimise. Indeed, not only the number of parameters to optimise at a time would be too large, but also it would mean to invert a $N(T-1) \times N(T-1)$ size matrix which is completely unrealistic. To avoid this, the estimation is performed in two steps.

First, the 18 autocorrelation coefficients for each station are estimated. For all $(t-1,t)$ such as $(j_{t-1} = (s,k), j_t = (s,l))$ Equation 4 written for a station x gives: $G_t(x) = a^s_{k,l}G_{t-1}(x) + E_t(x)$ where $E_t(x)$ is Gaussian noise with zero mean and variance $1-(a^s_{k,l}(x))^2$ and $a^s_{k,l}(x)$ is the autocorrelation at station x. Thanks to a composite censored likelihood each $a^s_{k,l}$ is estimated at each station x.

$$L^c(a^s_{k,l}(x)) = \prod_{t,t-1} L^c_{t,t-1}(a^s_{k,l}(x))$$

where $(t,t-1)$ such that $(j_t = (s,l), j_{t-1} = (s,k))$ and $L^c_{t,t-1}(a^s_{k,l}(x)) =$

$$\begin{cases} f_2(g_t(x), g_{t-1}(x)) & \text{if } g_t(x) > c_{j_t}(x), g_{t-1}(x) > c_{j_{t-1}}(x) \\ P(G_t(x) \leq c_{j_t}(x), G_{t-1}(x) \leq c_{j_{t-1}}(x)) & \text{if } g_t(x) \leq c_{j_t}(x), g_{t-1}(x) \leq c_{j_{t-1}}(x) \\ f_1(g_{t-1}(x))P(G_t(x) \leq c_{j_t}(x) | G_{t-1}(x) = g_{t-1}(x)) & \text{if } g_t(x) \leq c_{j_t}(x), g_{t-1}(x) > c_{j_{t-1}}(x) \\ f_1(g_t(x))P(G_{t-1}(x) \leq c_{j_{t-1}}(x) | G_t(x) = g_t(x)) & \text{if } g_t(x) > c_{j_t}(x), g_{t-1}(x) \leq c_{j_{t-1}}(x) \end{cases} \tag{5}$$

where f_2 a bivariate Gaussian density with zero mean, unit variance and covariance $a^s_{k,l}(x)$ and $P(G_t(x) \leq c_{j_t}(x), G_{t-1}(x) \leq c_{j_{t-1}}(x))$ is computed from the associated CDF. f_1 is the standard Gaussian density and the conditional probabilities above $P(G_t(x) \leq c_{j_t}(x) | G_{t-1}(x) = g_{t-1}(x))$ and $P(G_{t-1}(x) \leq$

$c_{j_{t-1}}(x)|G_t(x) = g_t(x))$ are respectively computed from the CDF $\mathcal{N}\left(a^s_{k,l}(x)g_{t-1}(x), 1-(a^s_{k,l}(x))^2\right)$ and $\mathcal{N}\left(a^s_{k,l}(x)g_t(x), 1-(a^s_{k,l}(x))^2\right)$ (the two latter distributions are obtained from the formulation given in Appendix B for the N-variate case applied to the bivariate case).

In Figure 3, the boxplots of the estimated parameters $\hat{a}^s_{k,l}(x)$ for each season and transitions are represented. In our model these coefficients are assumed to be constant over the region. To this end, the regional median of the estimated coefficients $\hat{a}^s_{k,l}(x)$ is taken.

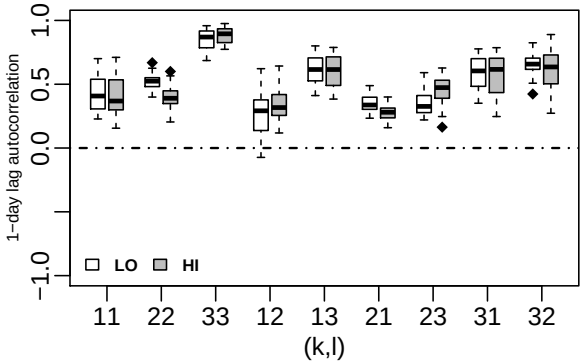


Figure 3: All stations boxplot 1-day lag autocorrelation coefficient $a^s_{k,l}$ estimated for each transition among GTs within a season.

Second, the parameters of the covariance function $\rho_j(\tau)$ for each sub-set j are separately estimated from the censored data $z_t(x) = \max(c_j(x), g_t(x))$, for t in sub-set j. In order to account for the temporal dependence between G_t and G_{t-1} in its estimation, spatial dependence is estimated from the Gaussian error E_t. Realisation of E_t are given by $\epsilon_t(\mathbf{x}) = g_t(\mathbf{x}) - \hat{a}^s_{k,l} \cdot g_{t-1}(\mathbf{x})$. Separate estimation of each ρ_j needs one more simplification. Indeed, for t in sub-set j the covariance E_t is $COV(E_t) = \Sigma_t - (\hat{a}^s_{k,l})^2\Sigma_{t-1}$. Here, the covariance is approximated by $COV(E_t) \approx \left(1-(\hat{a}^s_{k,l})^2\right)\rho_j$ by considering $\Sigma_{t-1} \approx \Sigma_t$.

ϵ_t is censored whenever g_t or g_{t-1} is. For a given day t in j_t, let $\mathcal{E}^o_t = \{x|g_t(x) > c_{j_t}(x)$ and $g_{t-1}(x) > c_{j_{t-1}}(x)\}$ be the ensemble of observed $\epsilon(x)$ and $\mathcal{E}^c_t = \{x|g_t(x) \leq c_{j_t}(x)$ and/or $g_{t-1}(x) \leq c_{j_{t-1}}(x)\}$ the ensemble of censored

$\epsilon(x)$. $\mathbf{e}_t$ is defined as the vector of censoring thresholds of $\epsilon_t(\mathbf{x})$ and β_j are the parameters of ρ_j. For E_t, several cases of censoring threshold $e_t(x)$ and hence of censoring intervals $\mathcal{I}_t^c(x)$ are possible. It depends on the sign of $a_{k,l}^s$ and whether or not $G_t(x)$ or $G_{t-1}(x)$ are censored. All the cases are given the Appendix C and their proportion are given in Table C.1. For a given day t in j_t, $\mathbf{I}_t^c = \{\mathcal{I}_t^c(x)\}$ is ensemble of censoring intervals of E_t.

According to Pesonen et al. (2015), for each sub-set j, since the $E_1, \ldots, E_T$ are independent, the censored likelihood of β_j given the $\{\epsilon_t(x)\}_{x \in \mathcal{E}_t^o}$ is:

$$L_j^c(\beta_j) = \prod_{t \in j} L_t^c(\beta_j). \tag{6}$$

For a given day t in sub-set j, the $L_t^c(\beta_j)$ can be written as following.

- If all the $\epsilon_t(x_i)$ are observed: $L_t^c(\beta_j) = f_N(\epsilon_t(x_1), \ldots, \epsilon_t(x_N); \beta_j) = f_N(\epsilon_t(\mathbf{x}); \beta_j)$. f_N is multivariate Gaussian density of dimension N.

- If at least one station is censored:

$$L_t^c(\beta_j) = f_o(\boldsymbol{\epsilon}_t^o) \cdot P(\mathbf{E}_t^c \in \mathbf{I}_t^c | \mathbf{E}_t^o = \boldsymbol{\epsilon}_t^o; \beta_j). \tag{7}$$

  $f_o(\boldsymbol{\epsilon}_t^o)$ is multivariate Gaussian density of dimension cardinal of $\mathcal{E}_{j_t}^o$, of zero mean and covariance $(1-(\hat{a}_{k,l}^s)^2)\rho_j$ when $j_{t-1} = (s,k)$ and $j_t = (s,l)$ (successive days in different seasons are omitted for simplicity). The probability in the right part of above equation is a Gaussian CDF since $\mathbf{E}_t^c | \mathbf{E}_t^o = \boldsymbol{\epsilon}_t^o$ is Gaussian (whose conditional mean and covariance formulation are given in Appendix B).

- If all the stations are censored: $L_t^c(\beta_j) = P(\mathbf{E}_t \in \mathbf{I}_t^c; \beta_j)$. This probability is the CDF of a N-variate Gaussian process, with zero mean and covariance $(1 - (\hat{a}_{k,l}^s)^2)\rho_j$.

Note that, the estimation of $\beta_1, \cdots, \beta_6$ by Equation 6 is only based on 59% of the observations according to Appendix C. Indeed, stations with consecutive dry days (case 1b) have no contributions to the likelihood of Equation 6. Thus, an alternative is suggested which consist in inferring the β_j directly from the

g_t and independently of the temporal dependence. Naturally, censoring cases still happen but the entire data-set is used. The $L_t^c(\beta_j)$ written for G_t take the following formulations:

$$\begin{cases} \phi_N(g_t(\mathbf{x});\beta_j) & \text{if} \quad \text{no station is censored,} \\ \phi_o(\mathbf{g}_t^o)\cdot P(\mathbf{G}_t^c \leq \mathbf{c}_{j_t}|\mathbf{G}_t^o = \mathbf{g}_t^o;\beta_j) & \text{if} \quad \text{at least one station is censored,} \\ P(\mathbf{G}_t \leq \mathbf{c}_{j_t};\beta_j) & \text{if} \quad \text{all stations are censored.} \end{cases}$$

where $\phi_o(\mathbf{g}_t^o)$ and $\phi_N(g_t(\mathbf{x}))$ are the multivariate Gaussian distribution associated to g_t. In that case, the $a_{k,l}^s$ are obviously omitted in the estimation of the β_j. Table C.1, gives the proportion of censored cases for this version. Hence, two versions of the model are compared: when ρ_j is estimated from either ϵ_t (taking into account the temporal correlation) or g_t (independently from the temporal correlation). Both alternatives are compared to the observations data.

3.4. Spatio-temporal rainfall simulations

The purpose of the study is to evaluate the ability of both versions of the model to reproduce the rainfall spatio-temporal properties given a GT. Thus, the objective is to compare the simulated rainfall density to the rainfall density of the past observation. Therefore, transitions between GTs are not modelled even if GT sequences can easily be generated thanks to a Markov model (*e.g.* Vrac et al., 2007; Ailliot et al., 2009). The simulations are performed using the observed sequence of GTs between 1969 and 2008 which is assumed to be long enough to contain a representative variety of transitions. The model applies for $t \geq 2$ only. For each day t:

1. if $t = 1$, $G_1(\mathbf{x})$ is randomly drawn from $\mathcal{N}_N(0, \Sigma_1)$,
2. if $t > 1$, $E_t(\mathbf{x})$ is randomly drawn from $\mathcal{N}_N(0, (1 - \hat{a}_{k,l}^s)\Sigma_t)$ and $G_t(\mathbf{x})$ is set to $\hat{a}_{k,l}^s G_{t-1}(\mathbf{x}) + E_t(\mathbf{x})$.

The simulations of the $E_t(\mathbf{x})$ are performed by eigenvalue decomposition of the covariance matrix. From the simulated $g_t(\mathbf{x})$, the $y_t(\mathbf{x})$ are retrieved from the inverse transformation of Equation 3. Note that in order to remove

the initialisation effect a warm-up is realised: the first year of simulation is discarded.

4. Simulations Evaluation

The model is evaluated in terms of precipitation intermittency, intensity and extreme properties. Using different indices the evaluation is made from three points of view: marginal, spatial and regional (or areal *i.e.* for aggregated rainfall over the catchment). Hundred simulations over 40 years (1969-2008) at the 47 stations (41 stations of the calibration set and 6 stations from the validation set) are performed for the two following versions of the model:

- AR1 p.exp: MAR(1) model with powered-exponential correlation function,
- AR1 p.expi: MAR(1) model with powered-exponential correlation function with independent estimation of the $a^s_{k,l}$ and ρ_j.

The simulations are confronted to the observed statistics.

4.1. Marginals properties

In this section two aspects of the model are evaluated: first the marginal distributions $\widehat{H}$ estimated from the data at the calibration stations and second the marginal distributions $\widetilde{H}$ obtained at the validation stations from the parameter mapping procedure. The evaluation is mostly made on the validation stations in order to assess the quality of the marginal parameters mapping. An article fully dedicated to the parameters mapping methodology used in this study is available in Blanchet et al. (2019). Only the results for AR1.pexp are shown here but the same conclusions are drawn for AR1.pexpi (as expected since the two versions differ only by the spatial correlation estimation).

Figure 4 gives, for both seasons and GT1, the daily mean (Mean), the wet-day mean (Mean>0, a day is considered wet at 0.1 mm) and the rainy day fraction (P1) for all stations (calibration set in grey and validation set in red).

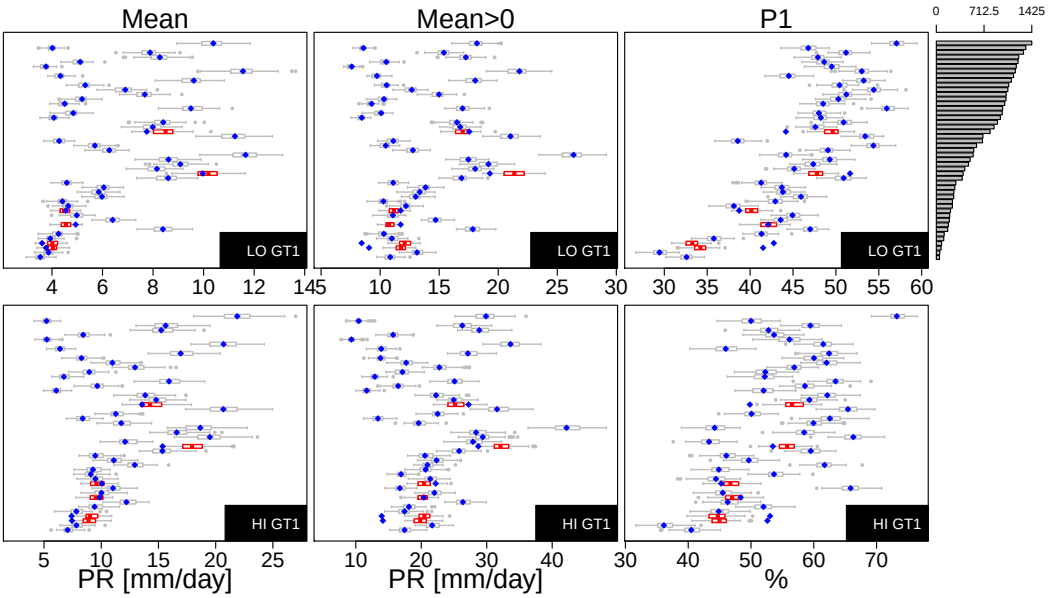


Figure 4: *Each colonne:* Mean (mm/day), mean of positive values (mm/day) and wet day fraction for GT1 and both seasons – *In line* grey: boxplot of 100 simulations, blue dots: observed statistics (ordered with respect to the altitude given by the barplot on the right). Red boxplots correspond to the simulations at the validation stations.

Little biases are only observed over the validation stations. Isolated stations situated on the edge of the domain and outside the catchment show the largest biases (*e.g.* Saint Julien de Peyrolas or Pont Saint Esprit). The geographical situation of these stations makes the interpolation more delicate due to the spatial extrapolation they require. Similar results are found for the other GTs. However no systematic (positive or negative) biases are noticed. This is something expected since the mapping model has been selected in Blanchet et al. (2019) as the best compromise over the entire domain. This is why, the interpolated parameters may not perfectly coincide with the at-site values but the differences remain low.

Figure 5 displays the monthly mean for the six validation stations for the AR1.pexp model. Note that, unlike the daily mean of Figure 4, the monthly mean also evaluates the temporal correlation.

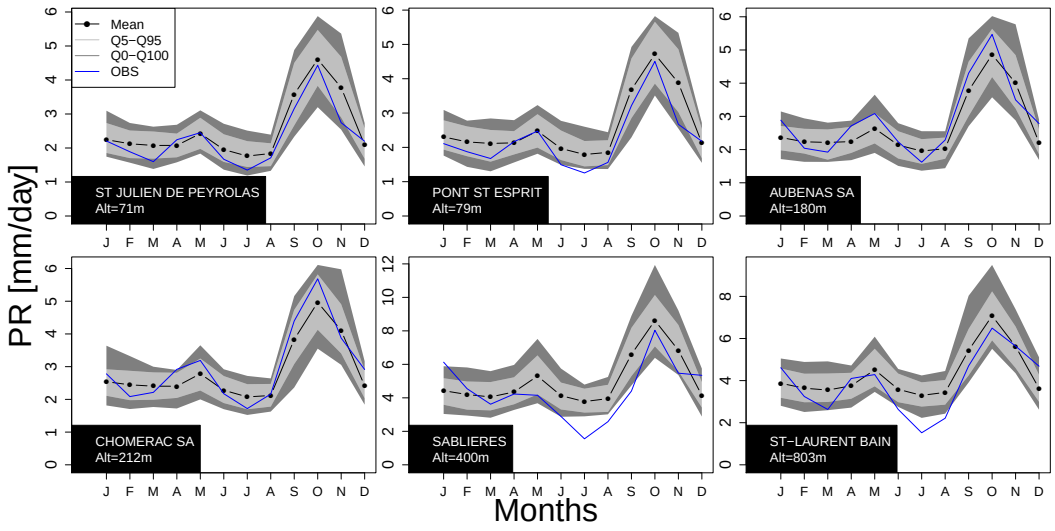


Figure 5: Daily mean of monthly precipitation at the validation stations. *Blue* the observations, *black dots* the mean of simulations, *light grey* (resp. dark grey) the 90% (resp. 100%) simulation intervals.

The precipitation seasonal aspect is important in terms of hydrological responses (e.g. Grouillet et al., 2016). In our model, precipitation seasonality is partly ensured by the frequency of the GTs. This modelling option combining the GT and the two really contrasted season correctly reproduces the seasonal cycle. For the four validation stations below 212m, the seasonal cycle is relatively well reproduced despite the biases noticed in Figure 4. For the two other stations it seems to be more difficult during Summer months. Similar behaviour to Sablières is observed for few calibration stations (not-shown) located on the north-western part of the domain (at higher altitudes) or in peculiar topographic area (*e.g.* a narrow valley). Even though these few stations, the use of GTs to condition the autocorrelation seems to be a good alternative with lower number of parameters than the classical monthly modelling (*e.g.*, Bennett et al., 2018) or lower constrain than the use of sine/cosine functions (*e.g.*, Kleiber et al., 2012; Baxevani and Lennartsson, 2015).

Stationary spatial models usually lack variability in annual precipitation to-

tals (*e.g.*, Wilks and Wilby, 1999; Mehrotra and Sharma, 2007; Bennett et al., 2018). The mean and the standard deviation of annual totals for each station are given in Figure 6. Annual total averages are well reproduced and the year-to-year variations of GT occurrence frequencies is enough to correctly reproduce the variability of the annual totals. Validation stations show little overestimations or underestimations of the annual totals caused by the interpolated marginal distributions as already stated for Figures 4. Some calibration stations underestimate the observed interannual variability. As previously, GT frequencies are not enough to represent all local year-to-year variations. In particular, for these sites, very high annual total values can be observed some years which can highly increase the standard variation of the observation. The stationary hypothesis of our model prevents to reproduce those peaks.

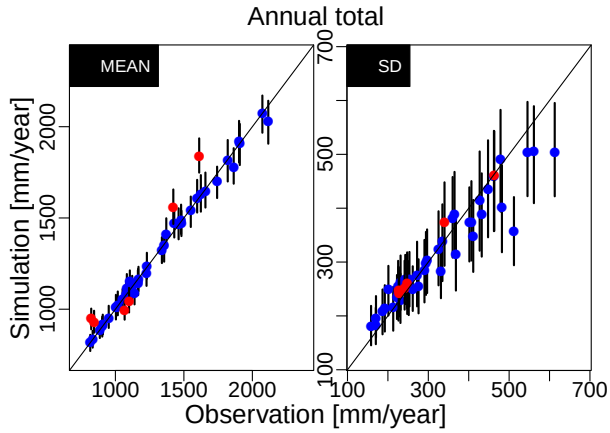


Figure 6: Interannual precipitation total mean *left* and standard deviation *right*. *Dots* Mean of simulations (*blue* dots for calibration stations, *red* dots for validation stations) and *black bars,* the 90% simulation intervals.

The presented model does not represent rain occurrence and rain persistence as specific parameters but implicitly by the censoring and the temporal autocorrelation of the latent Gaussian process. Dry and wet days persistences (spells) statistics are evaluated. Figure 7 represents the distributions of dry (Figure 7a.) and wet (Figure 7b.) spell duration (in days) for the six validation

stations. Both persistences are well reproduced with some underestimations and overestimations caused by the regionally constant $a^s_{k,l}$. By doing so, the model compromises on all stations which can induce a little too much or too low temporal correlation depending on the stations. Long duration spells ($\geq$ 10 days, representing less than 2%) seem to present larger overestimations, but this is a visual artifact introduced by the logarithmic scale.

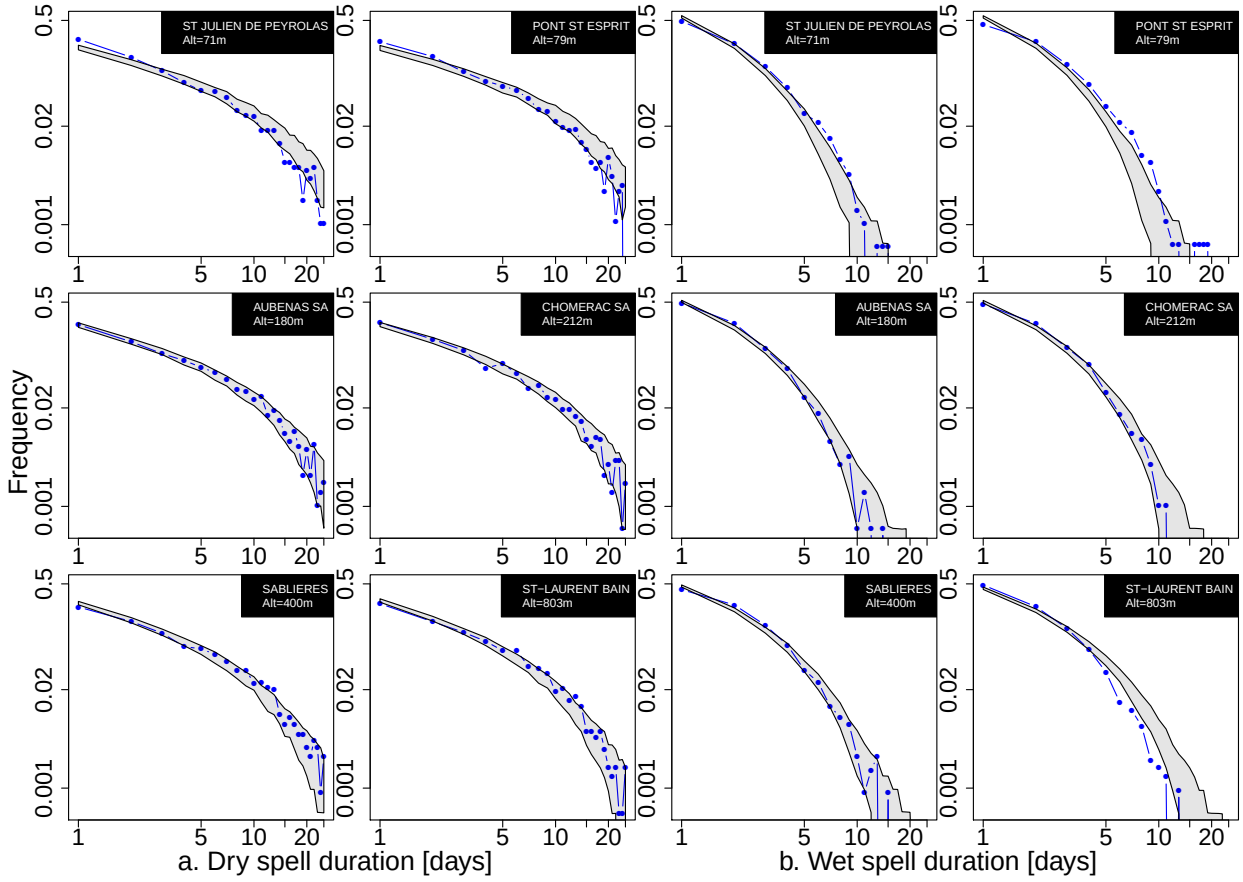


Figure 7: Distribution of spell lengths (in days) at the validation stations (log-log scale) - *Blue dots* Observations *grey,* the 90% simulation intervals. a. Dry spells - b. Wet spells.

The ability of the model to correctly represent the extremes is now assessed. Figure 8 shows the relative differences between the observation-based and simulation-based estimates of the 5-, 10-, 50- and 100-year return levels

of daily and 3-day cumulated rainfall. 3-day rainfall allows to examine the temporal autocorrelation and it is relevant from an hydrological point of view. Paquet et al. (2013) show for a quite similar catchment in terms size, topography and hydrological response that all significant floods are generated by 3-day sequences of intense precipitation. In order to have robust estimations of the return levels quantile, the return levels of Figure 8 are estimated by fitting the gamma mixture of Equation 2 over the simulations and observations of daily and 3-day rainfall. In order to apply the mixture to the 3-day rainfall a GT has to be affected to them. The this end, the most frequent GT during 3 days is affected to corresponding sequence. When three different GTs are observed during 3 days, the GT of the maximum during the sequence is affected to the sequence.

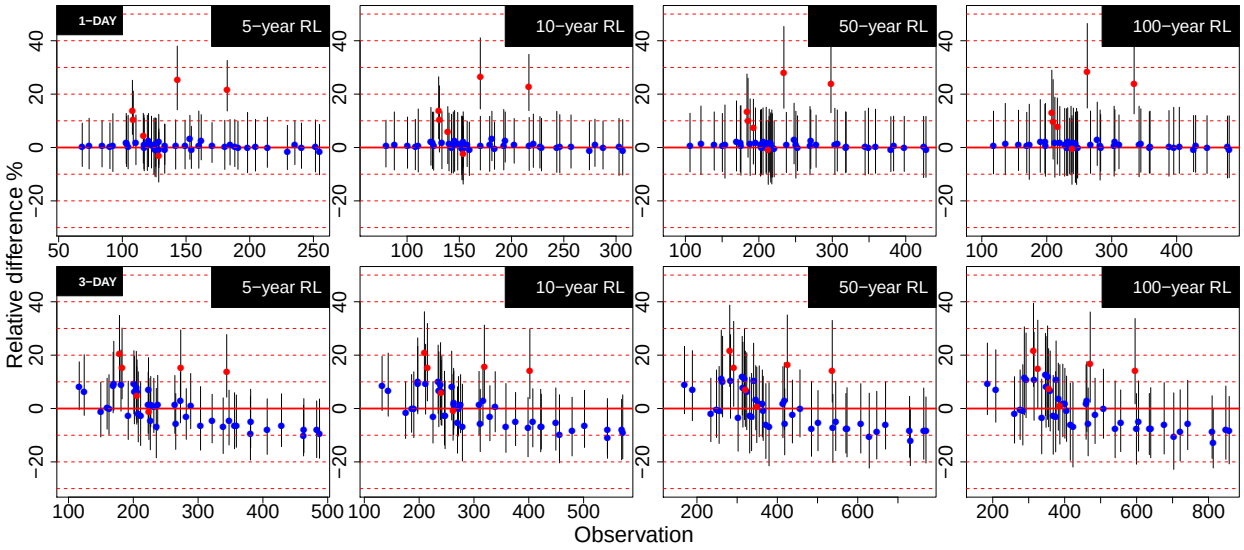


Figure 8: Relative differences (in %) of the estimated 5-, 10-, 50- and 100-year (from the left to the right) return levels between observed and simulated annual maxima for all stations with respect to the return levels (in mm) estimated over observations - *Dots* Mean of Simulations (*blue* calibration stations, *red* validation stations) *black bars,* the 90% simulation intervals. *Top*: 1-day rainfall *Bottom*: 3-day rainfall.

For the daily rainfall return levels, the relative differences are centred on

0 for the calibration stations. Positive biases are mostly observed for the validation stations (up to 30%), probably induced by the marginal parameters interpolation. The 3-day return level differences are larger (around 10%) with both underestimations (mainly for the largest estimated quantiles) and overestimations (mainly for the smallest estimated quantiles). The validation stations present the largest overestimations but close to the calibration stations (merely a little above 20%). Spatially uniform $a^s_{k,l}$ coefficients probably induce too much or too low temporal correlation depending on the stations.

4.2. Spatial properties

In this part, the ability of the model to correctly reproduce the inter-site dependence is evaluated. In all the following figures, the closer to the first bisector the model is, the better the model performs. In this section, and in the following ones the two methods for estimating the spatial dependence are confronted.

Figure 9 shows the Kendall rank correlation τ_k computed considering only the couples of positive rain amounts. The boxplots of the number of pair of stations simultaneously wet for each sub-set are shown in the first line. This number tends to be slightly underestimated for the AR1 p.exp version compared to the observations. This aspect is improved for the AR1 p.expi version. The model satisfyingly reproduces the correlation for the different sub-sets. In particular, it respects the decreasing spatial correlation from GT1 to GT3. The independent estimation (AR p.expi) considerably improves the correlation despite a slight underestimation. Larger underestimation in the correlation of the AR1 p.exp version is partly caused by the approximation that $\Sigma_{t-1} \approx \Sigma_t$ in the estimation of the spatial dependence (see Section 3.3.2) which may bias the estimation.

Recall that in the AR1 p.exp model, more than 41% of the censored cases fall in censored case 1b which has no influence on the covariance function estimation since the contribution of the corresponding terms in the censored likelihood is constant (see Appendix C for more details). Thus, estimation of the spatial

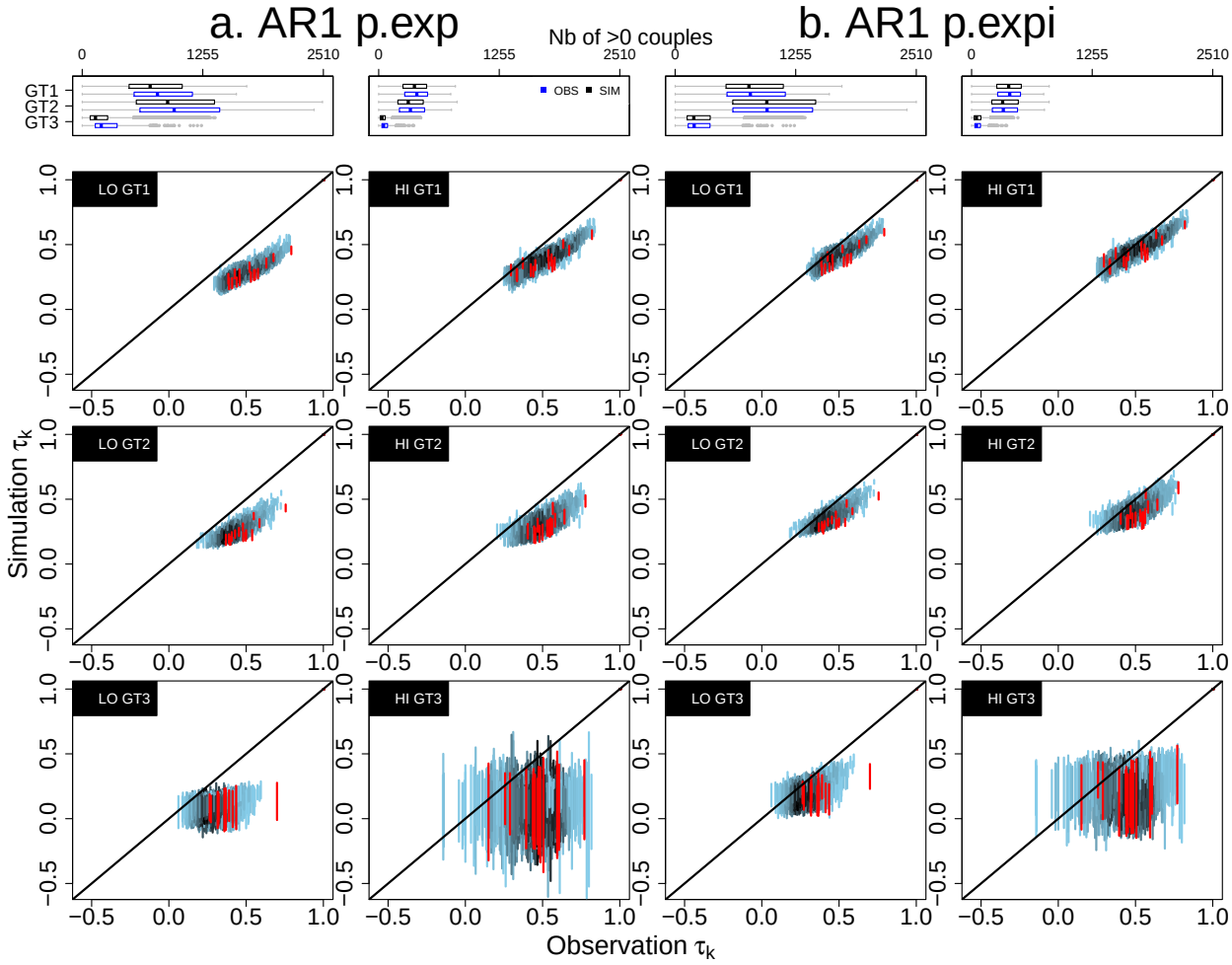


Figure 9: Pairwise Kendall correlation coefficient for each sub-set for positive rain amounts. Vertical color bars indicates the 90 % simulation intervals. Color shade from blue to black indicates the density of the plotted bars and red bars represent the probabilities for each pair of validation stations. a. AR1 p.exp - b. AR1 p.expi. This first line gives the boxplots of the number of pair of station simultaneously wet for each sub-set. *Blue* observed statistics - *Black* simulated statistics.

dependence in AR1 p.exp is actually based on much less data than for AR1 p.expi. In both versions of the model, one can notice that the correlation of simulations is almost constant for all pairs of stations for GT3. This sub-set

mainly regroups very localised rain events, which can explain the difficulty for the model to correctly estimate its spatial correlation. Besides, the number of jointly wet pairs is much lower for GT3 which introduces uncertainty in the computation of τ_k and makes its interpretation difficult. Validation stations (red segments) show similar behaviour to the calibration stations.

The spatial dependence of high quantiles is also investigated by computing the conditional probability of exceeding high quantile q. For two stations x_i and x_j, this probability is defined as $P_{1|1} = P\left[Y(x_i) > q_i | Y(x_j) > q_j\right]$. The $P_{1|1}$ associated to the 95th percentile are represented in Figure 10. The conclusions are similar to those drawn for τ_k with better performance for $P_{1|1}$ than for τ_k, although a larger variability can be noted for the simulations. For GT2 and GT3, the probabilities are better reproduced by AR1 p.expi while AR1 p.exp tends to underestimate those probabilities likewise for τ_k. For GT1, the probabilities are partly overestimated by AR1 p.expi while AR1 p.exp underestimates those of the LO season and better reproduces those of the HI season.

4.3. Areal properties

The model performance is analysed in terms of areal properties based on aggregated precipitation over the region (*i.e.* all station precipitations are cumulated). These are only computed over the calibration stations. The validation stations are excluded to avoid mixing with the potential error induced by the marginal mapping procedure.

The dry and wet spells distribution of the aggregated rainfall are represented in Figure 11 for both versions of the model. Wet and dry spells are very well reproduced by the AR1 p.expi version while AR1 p.exp slightly overestimates or underestimates the spell duration. Note that the spells are not explicitly prescribed in the model but rather induced by day-to-day correlation and the GT sequence. Spells are also investigated in some other studies using quite close modelling frameworks (*e.g.* Kleiber et al., 2012; Serinaldi and Kilsby, 2014). In those articles, the models show some difficulties to reproduce areal dry spells. However these studies consider wider areas (65 to 370 times larger than our

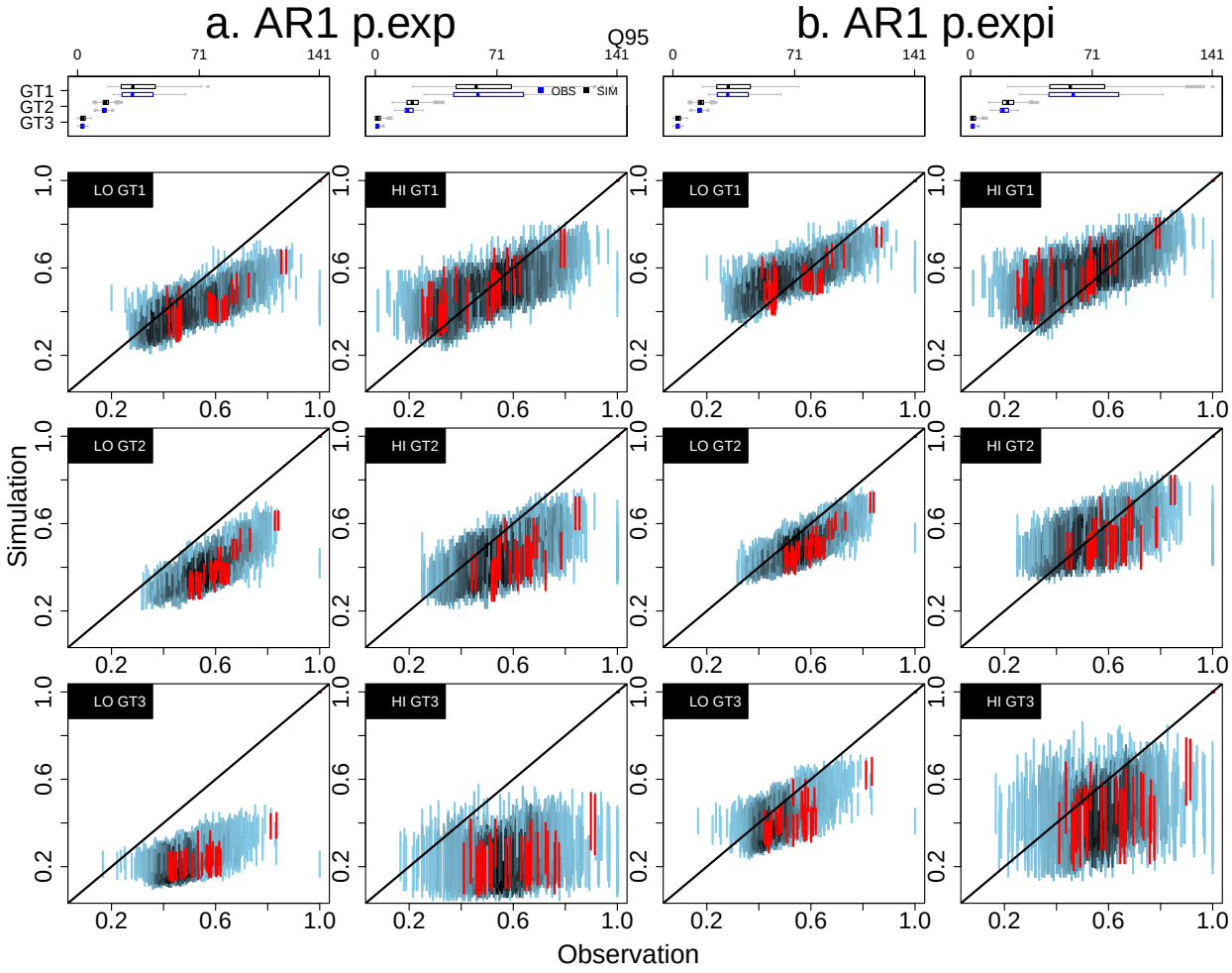


Figure 10: Empirical conditional excess probability $P_{1|1}$ for each sub-set and for 95% quantile. Vertical color bars indicates the simulation 90% intervals. Colour shade from blue to black indicates the density of the plotted bars and red bars represent the probabilities for each pair of validation stations. a. AR1 p.exp - b. AR1 p.expi. This first line gives the boxplots of the 95^{th} percentile at all stations for each sub-set. *Blue* observations - *Black* simulations.

study area) which can make this aspect more difficult to represent.

Figure 12 represents the distribution of jointly wet sites among the calibration stations. This shows the ability of the model to generate daily rain fields with the right size and at the right frequency. This criteria has been computed

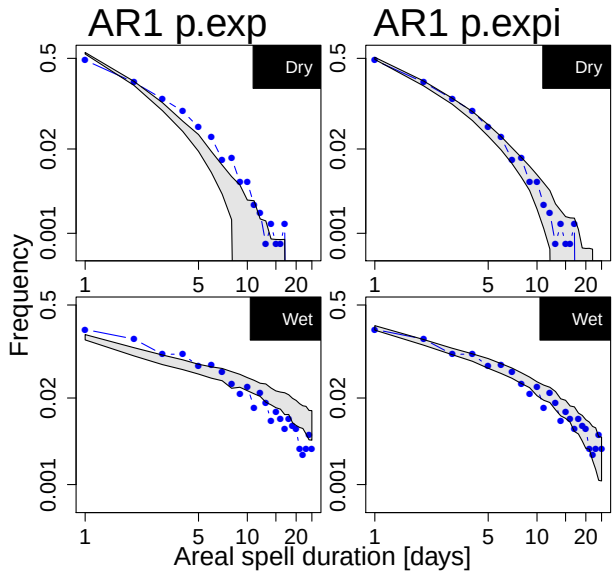


Figure 11: Distribution of spell lengths (in days) over the region (log-log scale). *Top*: Dry spells *Bottom*: Wet spells - *Blue dots* Observations *grey,* the 90% simulation intervals. *Left* AR1 p.exp - *Right* AR1 p.expi.

from the simulated data removing the values corresponding to missing value in the observations.

Globally, AR1 p.expi performs better. AR1 p.exp underestimates the frequency of the largest events and the frequency of the dry days while it overestimates the frequency of the intermediate size events. Similar results are obtained by Baxevani and Lennartsson (2015). The independent estimation reduces the bias in the largest and intermediate size events but it slightly overestimates the frequency of the small size events (< 5 stations) and the frequency of dry days.

Now the size of the events generating daily annual maxima is studied. Figure 13 shows for a given threshold the 90% range of areas (number of stations) experiencing rainfall no smaller than that threshold during the annual maximum events. The upper bound (resp. lower bound) of the envelope corresponds to the widest (smallest) area covered by a given magnitude or more. For both models and sub-sets, the lower bounds of the simulations match very well the

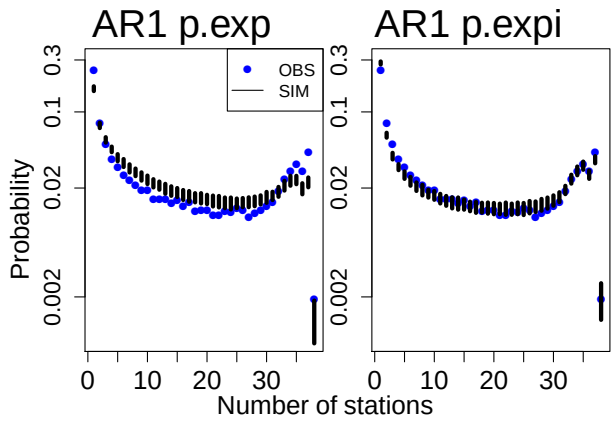


Figure 12: Distribution of jointly wet sites (log scale). *Blue dots*: Observation - *Black bars*: the 90% simulation intervals. *Left* AR1 p.exp - *Right* AR1 p.expi.

observations. Thus the least extended events are very well represented. The most extended events for a given magnitude (upper envelope) tend to be overestimated in size in GT1 during the HI season, while they tend to be underestimated in size in all the other subsets. The AR1 p.expi model slightly reduces the underestimation but slightly increases the overestimation in GT1 HI. Note that the GTs were defined in Blanchet et al. (2019) according to the spatial correlation of the WTs, with GT1 corresponding to the largest range of correlation, followed by GT2 and GT3. Figure 13 shows that the simulations correctly reproduce this aspect.

4.4. Model adaptability

The adaptability of the model to different catchments is a genuine issue. In order to illustrate the generality of the modelling framework, the exact same model as implemented for Ardèche is applied to a much bigger catchment within a different climatic region. The Durance catchment at Cadarache located in the southern French Alps is chosen (14,000 km^2 see Figure S1 of the supplementary material). The altitude of the region ranges up to 4000 m.a.s.l while the Ardèche catchment reaches around 1700 m.a.s.l. Fifty four stations with data from January 1, 1975 to December 31, 2014 are selected (for data availability see Figure

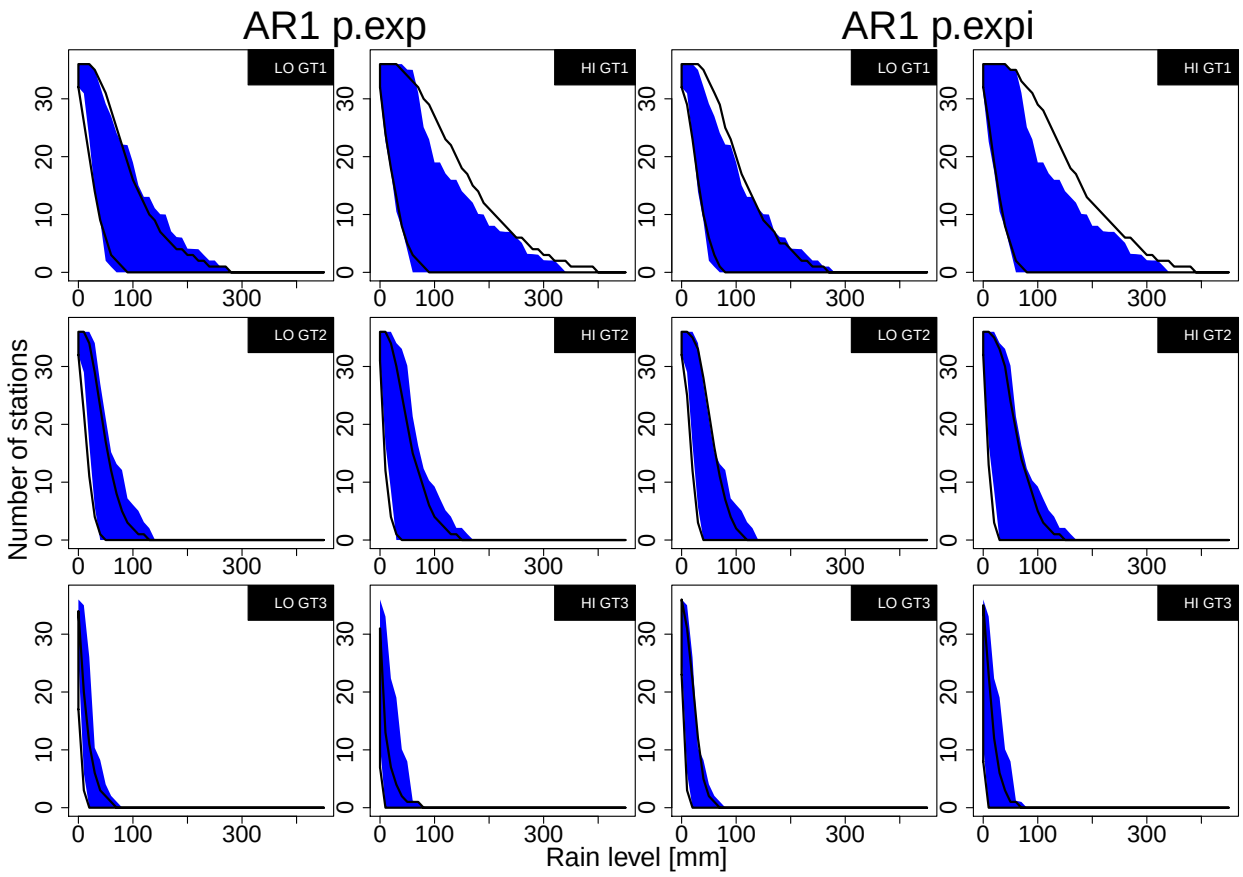


Figure 13: Number of stations (in ordinate) where it rains more than a given threshold (in abscissa) during the annual maximum events. *Blue*: Observation 90% intervals - *Black*: the simulation 90% intervals. *Left* AR1 p.exp - *Right* AR1 p.expi.

SA1 of the supplementary material). Table S1 (of the supplementary) gives the minimum, median and maximum of the annual and seasonal averages of daily non-zero rainfall of the 54 stations. The daily average of rain intensity over the Durance catchment is half to 2/3 of the daily average of rain intensity over the Ardèche. GT1 and GT2 have almost the same rain intensity while it is more contrasted for Ardèche. No validation stations are considered for this catchment since the generality of the selection framework of the marginal distribution and the parameter interpolation is thoroughly discussed in Blanchet et al. (2019).

The same seasons, GTs (based on the spatial correlation of rain amount over the Ardèche) and the best model version (AR1 p.expi) used for the Ardèche are adopted. Figures 3 to 13 are reproduced for the Durance catchment and given in the supplementary material (Figures S2 to S12). Between the two catchments, only few differences of performance are observed in terms of marginal properties. In particular, there are differences in the standard deviation of annual totals, the wet spells duration and 3-days return levels (respectively Figure S5, S6 and S7 of the supplementary material). The variability of annual totals seems to be mostly slightly overestimated while there are over- and underestimations for Ardèche. The frequency of the large wet spells (>5 days, they represent less than 2%) are a little overestimated for almost all stations while there are over- and under-estimations for Ardèche. Similarly, the 3-day return levels are systematically overestimated (up to a little above 20%) for the Durance catchment. The conclusions for all the other marginal properties, the spatial properties and areal properties (Figures S2 to S4 and S8 to S12) are the same for both catchments. The differences in the model performance between the two catchment may probably be linked to the sub-sampling in seasons/GTs. The sub-sampling for the Ardèche catchment may not be totally suited to the Durance catchment.

It is quite remarkable that the performance of the model over such different catchments is globally similar. This proves that the proposed model combining weather pattern with a latent Gaussian field is general enough to be applied to any region, although some modelling choices (sub-sampling, marginal distribution, spatial and temporal correlation) may need to be tailored for some regions.

5. Conclusions, discussions and perspectives

5.1. Conclusions

The aim of this study is to develop a high resolution spatial rainfall model from station data in order to generate spatially distributed rainfall scenarios for

hydrological applications based on a distributed rainfall-runoff model. To this end, the modelling strategy relies on weather types sub-sampling conditionally on which a first order Markovian autoregressive model is calibrated. An application of the model is performed over the Ardèche catchment situated in south of France. Given the complex terrain nature and the strong variability of the rainfall, this catchment constitutes a challenging candidate to test the model. The added-value of combining sub-sampling with spatial modelling is evaluated with regards to the observations. Two versions of the model are compared considering three aspects: the marginal, spatial and areal properties.

The at-site behaviour is assessed in terms of daily occurrence, rainfall intensity (at daily, monthly and annual scale), persistence and extremes. Results are globally satisfying for both calibration and validation stations. Indeed, the marginal distribution parameters interpolation seems to be efficient and shows little discrepancies. The discrepancies of the marginal properties have mainly three sources: (i) the interpolated margins (illustrated by the biases on the validation stations Figures 4 and 8), (ii) the constant temporal correlation over the region can induce local-scale autocorrelation discrepancies (see for instance the return levels of 3-day cumulated rainfall for large return periods Figure 8) and (iii) the sub-sampling in two seasons and three weather types is not always enough to represent the seasonality or the year-to-year variability (Figures 5 and 6). As mentioned in Blanchet et al. (2019), the mapping process of the margins is still perfectible. For instance, in order to take into account complex orography or climate non-stationarity, covariates characterising the terrain nature (Carreau et al., 2013) or atmospheric circulation (Serinaldi and Kilsby, 2014) can be introduced. This could improve the quality of the model in terms of seasonality and variability. However, this would imply an heavier parametrisation and a substantial work is needed to adapt the parameter mapping procedure in a temporal non-stationary context.

The reproduction of inter-site dependence is also studied. Two versions of the model are confronted: one in which the spatial dependence is estimated conditionally on temporal correlation (AR1 p.exp) and the other one in which

the spatial and temporal correlation are estimated independently (AR1 p.expi). The dependence is modelled by a powered-exponential correlation function. The dependence is examined with respect to daily rainfall and high quantiles. Results show that AR1 p.expi reproduces better the inter-site dependence despite a slight tendency to underestimation. The better performance of AR1 p.expi is probably because its estimation involves actually more data than AR1 p.exp.

The areal aspect of the aggregated precipitation over the area is assessed. The model shows good performance with even better results for the AR1 p.expi version. And finally, the hybrid model developed in this study present the advantage to work for different catchment within different climatic regions with very little alterations.

Rain fields generated over a regular grid of one square kilometre spatial resolution for the Ardèche catchment are given in an animated plot supplied in the supplementary material.

5.2. Discussions and perspectives

Despite the good performance of the AR1 p.expi version, it slightly underestimates the spatial correlation. This can have four causes:

1. the data sub-sampling into two seasons and three GTs might be relevant for the rain intensity over the region but not necessarily optimal for the spatial dependence. Indeed, GTs are obtained by grouping the WTs according to the spatial correlation. The WTs are based on the clustering of the geopotential heights which has proved itself to be relevant for rain intensity (Garavaglia et al., 2010) but these have not been validated for the spatial dependence,
2. the use of the meta-Gaussian framework causes potential correlation reduction when the marginals are transformed from Gaussian to rainfall marginals. This theoretical aspect has been proven by Kendall et al. (1979) and Matheron (1989). Some solutions have been proposed to inflate the Gaussian correlation in order to compensate the correlation reduction. Li and Hammond (1975) is one of the first study addressing this issue. In

the case of rainfall Guillot (1999) and Leblois and Creutin (2013) used a polynomial expansion while Papalexiou (2018) proposed a simpler parametric transformation to inflate the correlation. However in our case it represents a huge numerical effort for unguaranteed improvements and new developments are still needed to fit our purposes,

3. the simplification of the covariance of the noise term E_t in order to estimate the correlation function independently for each sub-set. The considered simplification $\Sigma_t = \Sigma_{t-1}$ is only true 70% of the times, which probably biases the estimation. Relaxing this hypothesis would be theoretically possible, but the estimation would be a burden,

4. the use of a latent Gaussian process which is radially symmetric. This means that in the case of a Gaussian process $\mathbf{G}$ with zero mean and covariance matrix Σ and for any vector $\mathbf{u} = (u_1, \cdots, u_N) \in [0,1]^N$, we have: $P(G_1 \leq \Phi^{-1}(u_1), \cdots, G_N \leq \Phi^{-1}(u_N)) = P(G_1 > \Phi^{-1}(1-u_1), \cdots, G_N > \Phi^{-1}(1-u_N))$.

This last point is empirically illustrated in Figure 14, for $u_k = p_j^0(x_k)$ in sub-set j corresponding to the high-risk season and GT1 which is the sub-set containing the most stations (x_k, x_l) with $p_j^0 < 0.5$. For each pair of stations, the joint empirical probability of non-exceedance $NEP_{kl} = P(Y(x_k) = 0, Y(x_l) = 0)$ and exceedance $EP_{kl} = P(Y(x_k) > H^{-1}_{Y_j(x_k)}(1 - p_j^0(x_k)), Y(x_l) > H^{-1}_{Y_j(x_l)}(1 - p_j^0(x_l)))$ are computed. Figure 14 represents the differences $EP_{ij} - NEP_{ij}$ for the model AR1 p.expi versus the observations.

For the observations, $EP - NEP$ is mostly positive and depends on the pair of stations. This means that the bivariate CDF of precipitation is mainly right skewed and the asymmetry is spatially non-stationary. On the contrary, for the simulations $EP - NEP$ is constant around zero which is prescribed by the Gaussian process.

In order to introduce asymmetry, other spatial dependence structure can be considered. For instance, the chi-square copula introduced by Bàrdossy (2006) and recently explored by Quessy et al. (2016) allows to prescribe the asymmetry.

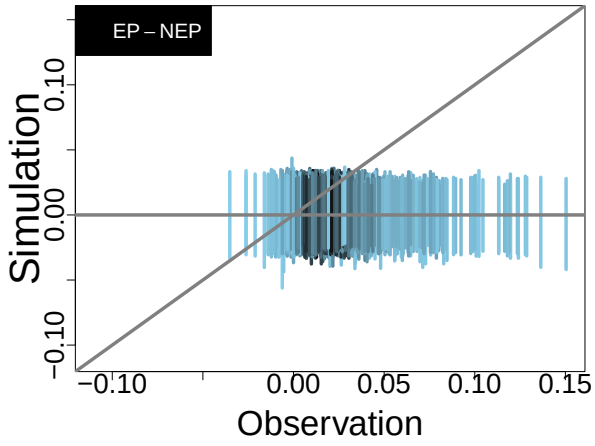


Figure 14: Difference between the pairwise joint exceedance probability (EP) and pairwise joint non-exceedance probability (NEP) of the simulations versus EP-NEP for the observation. The vertical color bars indicates the 90% simulation intervals. The color shade from blue to black indicates the density of the plotted bars

Favre et al. (2018) have proposed a generalisation of this copula allowing for upper tail dependence. However their use in a spatial rather than multivariate context poses some difficulties, in particular with regards to the estimation of the correlation function (cf. Nelsen, 2007; Joe, 2014, for more details). Exploring the added-value of different copulas prescribing asymmetry would be relevant.

Concerning the estimation of the spatio-temporal dependence, simplifications have been made to the MAR(1). The first simplification states that the temporal correlation is constant over the region. In principle, $a^s_{k,l}$ can vary in space but this complicates the estimation procedure. First, if the matrix $A_{t,t-1}$ has different coefficients on its diagonal, the matrix $(Id_N - A^2_{t,t-1})\Sigma_{j_t}$ is not symmetrical. Thus, additional constraints on the $a^s_{k,l}$ have to be set to make the matrix $(Id_N - A^2_{t,t-1})\Sigma_{j_t}$ symmetric. This can be easily done for 41 stations but it is not realistic for high resolution fields due to computational time and numerical problems. Second, in the view of generating rain fields with spatially varying a, these parameters have to be mapped similarly to the marginal parameters (Blanchet et al., 2019). However, spatial patterns are not obvious

for all transitions (not-shown) and a tricky interpolation is avoided by taking it to be spatially uniform. To summarize, the use of diagonal matrix $A_{t,t-1}$ reproduces only the lag 0 spatial correlation and lag-1 autocorrelation. This modelling choice does not reproduce the rain fields advection (or movement), which may be necessary for hourly data but is less important for daily data and is omitted here for computational reasons.

The second simplification is to consider separately the temporal and the spatial dependence. Spatio-temporal correlation function can be used to simultaneously estimate both dependencies (cf. Cressie and Wikle, 2011; Bourotte et al., 2016, for example). However, in that case the use of a censored likelihood is not realistic. Most of the times, a pairwise composite likelihood or a method of moment is used (*e.g.* Baxevani and Lennartsson, 2015; Bourotte et al., 2016).

Concerning the weather pattern-based sub-sampling, instead of using synoptic WT, a direct clustering of days with similar spatial correlation could improve the model performance. A solution would be to cluster days based not only on synoptic variables but also including indices of the spatial variability of rainfall. The rainfall variability can be assessed through indicators such as the number of wet stations, where the rainfalls are located (on the foothills, the ridge or the plateau) or the rain field orientation. A methodology inspired from studies conducted over radar data could be adapted in our case (*e.g.* Benoit et al., 2018b).

An additional model deserves to be added, to simulate long WT sequences instead of repeating the observed 40 year sequences as it is done in the article. For hydrological applications, it should be able to model the correct frequency of occurrence of each GT within each month of the year, and also the correct distribution of WT spells. A first order Markov with covariates, accounting for monthly variations of GTs occurrence, may be a relevant option to achieve this.

Last but not least, considering the relatively small size and the strong orographic orientation of our study catchment, there is no evidence of non-stationary spatial dependence. However, if larger domains are considered, non-stationarity can be suspected in the spatial dependence. Many ways are possible

to introduce non-stationarity (cf. Risser, 2015, for a review). A promising way for mountain catchments with complex topography (*e.g.* in the Alps) would be to use a non-stationary covariance function. Paciorek and Schervish (2006) give a formulation for a Gaussian process allowing to derive a non-stationary covariance function from a stationary one.

Acknowledgments

The authors wish to acknowledge Météo France for the rainfall data used in this study. These data have been transmitted to EDF during the EXTRAFLO project (2009-2013). The dataset used in this study has been provided to the authors by EDF and Météo-France for this research. It could be made available to other researchers under a specific research agreement. Requests should be sent to dtg-demande-donnees-hydro@edf.fr.

Appendix A. Data availability

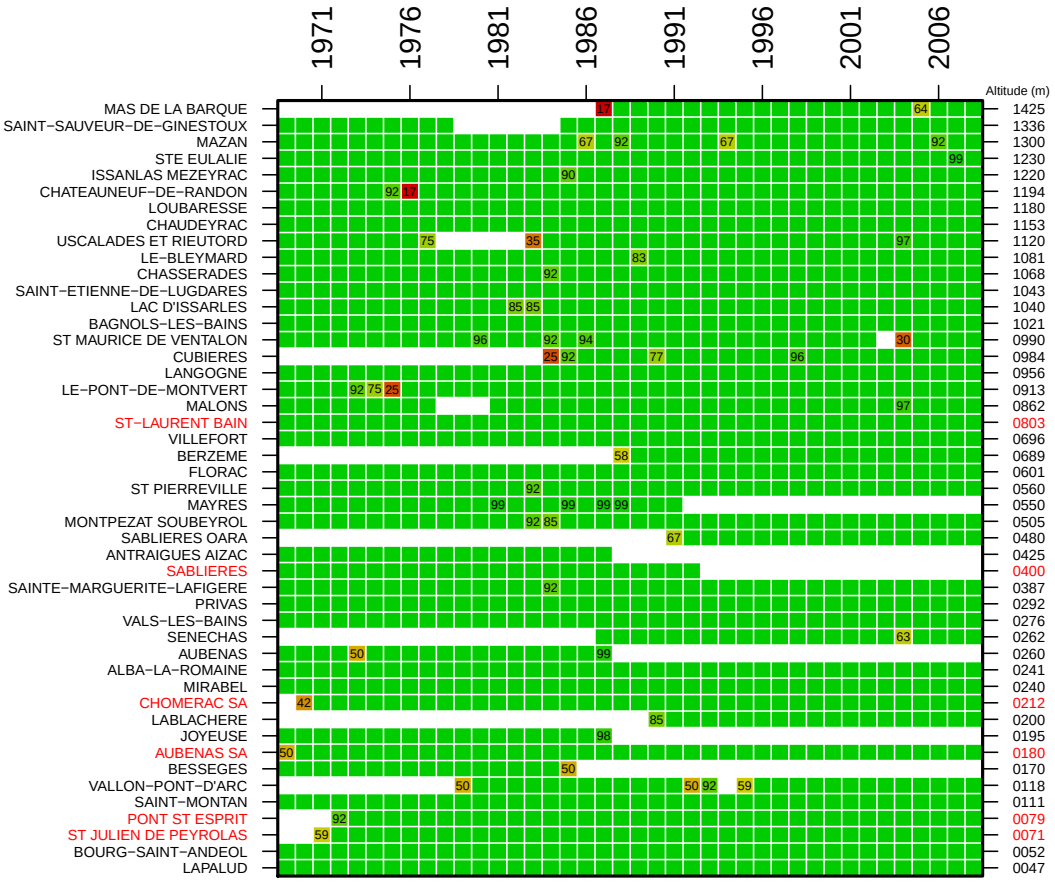


Figure A.1: Data availability - Green: complete years. White: empty years. Other colors: year with missing values, the percentage of available data are indicated. Station are ordered with respect to the altitude.

Appendix B. Conditional moments of Gaussian process.

Let U be a N-variate Gaussian with zero mean and covariance matrix Σ and U_1, U_2 be sub-vectors of respective dimensions $P+Q=N$ such as $U=[U_1,U_2]$

and

$$\Sigma = \begin{bmatrix} \Sigma_{11} & \Sigma_{21}^T \\ \Sigma_{21} & \Sigma_{22} \end{bmatrix}.$$

Then the conditional distribution $U_2|U_1 = u_1$ is Gaussian with the following mean vector $\mu_{2|1}$ and covariance matrix $\Sigma_{2|1}$:

$$\begin{aligned} \mu_{2|1} &= \Sigma_{21}\Sigma_{11}^{-1} \times u_1 \\ \Sigma_{2|1} &= \Sigma_{22} - \Sigma_{21}\Sigma_{11}^{-1}\Sigma_{21}^T \end{aligned}$$

Appendix C. E_t censoring interval cases.

For a given day t, there are three possible censoring interval $\mathcal{I}_t^c(x)$ for each station $x \in \mathcal{E}_t^c$:

1. If both $g_t(x)$ and $g_{t-1}(x)$ are censored then $g_t(x) \leq c_{j_t}(x)$ and $g_{t-1}(x) \leq c_{j_{t-1}}(x)$:
   (a) if $a < 0$ then $\epsilon_t(x) \leq c_{j_t}(x) - a \cdot c_{j_{t-1}}(x) = e_t(x) \Longrightarrow \mathcal{I}_t^c(x) = [-\infty, e_t(x)]$
   (b) if $a > 0$ then $\mathcal{I}_t^c(x) = [-\infty, \infty]$[1]
2. If only $g_{t-1}(x)$ is censored then $g_{t-1}(x) \leq c_{j_{t-1}}(x)$:
   (a) if $a < 0$ then $\epsilon_t(x) \leq g_t(x) - a \cdot c_{j_{t-1}}(x) = e_t(x) \Longrightarrow \mathcal{I}_t^c(x) = [-\infty, e_t(x)]$
   (b) if $a > 0$ then $\epsilon_t(x) \geq g_t(x) - a \cdot c_{j_{t-1}}(x) = e_t(x) \Longrightarrow \mathcal{I}_t^c(x) = [e_t(x), \infty]$
3. If only $g_t(x)$ is censored then $g_t(x) \leq c_{j_t}(x)$:
   - $\epsilon_t(x) \leq c_{j_t}(x) - a \cdot g_{t-1}(x) = e_t(x) \Longrightarrow \mathcal{I}_t^c(x) = [-\infty, e_t(x)]$

For each day t, a vector $\mathbf{e_t} = \{e_t(x)\}$ with its associated censoring interval is obtained.

Table C.1 gives the percentage of each censoring cases that are encountered when ρ_j is estimated from ϵ_t. C gives the total percentage of censored cases.

[1] these cases have no contribution to the likelihood of Equation 6, since $P(E_t^c(x) \in \mathcal{I}_t^c(x); \beta_j) = 1$ whatever β_j independent from covariance

Table C.1: Percentage of censoring.

Cases	1a	1b	2a	2b	3	C	NC
ϵ_t	0%	41.44%	0%	12.34%	12.34%	66.12%	33.88%
g_t	-	-	-	-	-	63.64%	36.36%

NC regroups all uncensored cases where it rains everywhere at t and $t-1$. The main information here is that more than 41% of the $\epsilon_t(x)$ are in the case 1b, corresponding to successive dry days, which does not contribute to the likelihood of ρ_j. The fraction of censored (C) and uncensored (NC) stations are also given when ρ_j is estimated from g_t.

List of Figures

1 Map of the studied region. Superficie: 2,260 km^2 – 47 Stations – Station elevation: from 47 to 1425 m – Red stations are validation stations. 8

2 Schematic summary of the full estimation and simulation process. 11

3 All stations boxplot 1-day lag autocorrelation coefficient $a^s_{k,l}$ estimated for each transition among GTs within a season. 17

4 *Each colonne:* Mean (mm/day), mean of positive values (mm/day) and wet day fraction for GT1 and both seasons – *In line* grey: boxplot of 100 simulations, blue dots: observed statistics (ordered with respect to the altitude given by the barplot on the right). Red boxplots correspond to the simulations at the validation stations. 21

5 Daily mean of monthly precipitation at the validation stations. *Blue* the observations, *black dots* the mean of simulations, *light grey* (resp. dark grey) the 90% (resp. 100%) simulation intervals. 22

6 Interannual precipitation total mean *left* and standard deviation *right*. *Dots* Mean of simulations (*blue* dots for calibration stations, *red* dots for validation stations) and *black bars,* the 90% simulation intervals. 23

7 Distribution of spell lengths (in days) at the validation stations (log-log scale) - *Blue dots* Observations *grey,* the 90% simulation intervals. a. Dry spells - b. Wet spells. 24

8 Relative differences (in %) of the estimated 5-, 10-, 50- and 100-year (from the left to the right) return levels between observed and simulated annual maxima for all stations with respect to the return levels (in mm) estimated over observations - *Dots* Mean of Simulations (*blue* calibration stations, *red* validation stations) *black bars,* the 90% simulation intervals. *Top*: 1-day rainfall *Bottom*: 3-day rainfall. 25

9 Pairwise Kendall correlation coefficient for each sub-set for positive rain amounts. Vertical color bars indicates the 90 % simulation intervals. Color shade from blue to black indicates the density of the plotted bars and red bars represent the probabilities for each pair of validation stations. a. AR1 p.exp - b. AR1 p.expi. This first line gives the boxplots of the number of pair of station simultaneously wet for each sub-set. *Blue* observed statistics - *Black* simulated statistics. 27

10 Empirical conditional excess probability $P_{1|1}$ for each sub-set and for 95% quantile. Vertical color bars indicates the simulation 90% intervals. Colour shade from blue to black indicates the density of the plotted bars and red bars represent the probabilities for each pair of validation stations. a. AR1 p.exp - b. AR1 p.expi. This first line gives the boxplots of the 95^{th} percentile at all stations for each sub-set. *Blue* observations - *Black* simulations. 29

11 Distribution of spell lengths (in days) over the region (log-log scale). *Top*: Dry spells *Bottom*: Wet spells - *Blue dots* Observations *grey*, the 90% simulation intervals. *Left* AR1 p.exp - *Right* AR1 p.expi. 30

12 Distribution of jointly wet sites (log scale). *Blue dots*: Observation - *Black bars*: the 90% simulation intervals. *Left* AR1 p.exp - *Right* AR1 p.expi. 31

13 Number of stations (in ordinate) where it rains more than a given threshold (in abscissa) during the annual maximum events. *Blue*: Observation 90% intervals - *Black*: the simulation 90% intervals. *Left* AR1 p.exp - *Right* AR1 p.expi. 32

14 Difference between the pairwise joint exceedance probability (EP) and pairwise joint non-exceedance probability (NEP) of the simulations versus EP-NEP for the observation. The vertical color bars indicates the 90% simulation intervals. The color shade from blue to black indicates the density of the plotted bars 37

A.1 Data availability - Green: complete years. White: empty years. Other colors: year with missing values, the percentage of available data are indicated. Station are ordered with respect to the altitude. 40

References

Ailliot, P., Allard, D., Monbet, V., Naveau, P., 2015. Stochastic weather generators: an overview of weather type models. Journal de la Société Française de Statistique 156, 101–113.

Ailliot, P., Thompson, C., Thomson, P., 2009. Space–time modelling of precipitation by using a hidden markov model and censored gaussian distributions. Journal of the Royal Statistical Society: Series C (Applied Statistics) 58, 405–426. doi:10.1111/j.1467-9876.2008.00654.x.

Ambrosino, C., Chandler, R., Todd, M., 2014. Rainfall-derived growing season characteristics for agricultural impact assessments in south africa. Theoretical and Applied Climatology 115, 411–426. doi:10.1007/s00704-013-0896-y.

Bàrdossy, A., 2006. Copula-based geostatistical models for groundwater quality parameters. Water Resources Research 42, W11416. doi:10.1029/2005WR004754.

Bàrdossy, A., Pegram, G.G.S., 2009. Copula based multisite model for daily precipitation simulation. Hydrology and Earth System Sciences 13, 2299–2314. doi:10.5194/hess-13-2299-2009.

Baxevani, A., Lennartsson, J., 2015. A spatiotemporal precipitation generator based on a censored latent gaussian field. Water Resources Research 51, 4338–4358. doi:10.1002/2014WR016455.

Bellone, E., Hughes, J.P., Guttorp, P., 2000. A hidden markov model for downscaling synoptic atmospheric patterns to precipitation amounts. Climate Research 15, 1–12.

Bennett, B., Thyer, M., Leonard, M., Lambert, M., Bates, B., 2018. A comprehensive and systematic evaluation framework for a parsimonious daily rainfall field model. Journal of Hydrology 556, 1123 – 1138. doi:https://doi.org/10.1016/j.jhydrol.2016.12.043.

Benoit, L., Allard, D., Mariethoz, G., 2018a. Stochastic rainfall modeling at sub-kilometer scale. Water Resources Research 54, 4108–4130. doi:10.1029/2018WR022817.

Benoit, L., Vrac, M., Mariethoz, G., 2018b. Dealing with non-stationarity in sub-daily stochastic rainfall models. Hydrology and Earth System Sciences 22, 5919–5933. doi:10.5194/hess-22-5919-2018.

Blanchet, J., Creutin, J.D., 2017. Co-occurrence of extreme daily rainfall in the French Mediterranean region. Water Resources Research 53, 9330–9349. doi:10.1002/2017WR020717.

Blanchet, J., Paquet, E., Vaittinada Ayar, P., Penot, D., 2019. Mapping rainfall hazard based on rain gauge data: an objective cross-validation framework for model selection. Hydrology and Earth System Sciences 23, 829–849. doi:10.5194/hess-23-829-2019.

Bourotte, M., Allard, D., Porcu, E., 2016. A flexible class of non-separable cross-covariance functions for multivariate space–time data. Spatial Statistics 18, 125 – 146. doi:https://doi.org/10.1016/j.spasta.2016.02.004.

Buishand, T.A., Brandsma, T., 2001. Multisite simulation of daily precipitation and temperature in the rhine basin by nearest-neighbor resampling. Water Resources Research 37, 2761–2776. doi:10.1029/2001WR000291.

Burton, A., Fowler, H.J., Kilsby, C.G., O'Connell, P.E., 2010. A stochastic model for the spatial-temporal simulation of nonhomogeneous rainfall occurrence and amounts. Water Resources Research 46, W11501. doi:10.1029/2009WR008884.

Caraway, N.M., McCreight, J.L., Rajagopalan, B., 2014. Multisite stochastic weather generation using cluster analysis and k-nearest neighbor time series resampling. Journal of Hydrology 508, 197 – 213. doi:https://doi.org/10.1016/j.jhydrol.2013.10.054.

Carreau, J., Neppel, L., Arnaud, P., Cantet, P., 2013. Extreme rainfall analysis at ungauged sites in the south of france: comparison of three approaches. Journal de la Société Française de Statistique 154, 119–138.

Chandler, R.E., 2002. Glimclim: generalized linear modelling for daily climate time series—user guide. Tech rep. Department of Statistical Science, University College London doi:10.1029/2001WR000906.

Cressie, N., Wikle, C.K., 2011. Statistics for spatio-temporal data. Wiley, Hoboken, New Jersey.

Delrieu, G., Nicol, J., Yates, E., Kirstetter, P.E., Creutin, J.D., Anquetin, S., Obled, C., Saulnier, G.M., Ducrocq, V., Gaume, E., Payrastre, O., Andrieu, H., Ayral, P.A., Bouvier, C., Neppel, L., Livet, M., Lang, M., du Châtelet, J.P., Walpersdorf, A., Wobrock, W., 2005. The catastrophic flash-flood event of 8–9 september 2002 in the gard region, france: A first case study for the cévennes–vivarais mediterranean hydrometeorological observatory. Journal of Hydrometeorology 6, 34–52. doi:10.1175/JHM-400.1.

Drobinski, P., Ducrocq, V., Alpert, P., Anagnostou, E., Béranger, K., Borga, M., Braud, I., Chanzy, A., Davolio, S., Delrieu, G., Estournel, C., Boubrahmi, N.F., Font, J., Grubišić, V., Gualdi, S., Homar, V., Ivančan-Picek, B., Kottmeier, C., Kotroni, V., Lagouvardos, K., Lionello, P., Llasat, M.C., Ludwig, W., Lutoff, C., Mariotti, A., Richard, E., Romero, R., Rotunno, R., Roussot, O., Ruin, I., Somot, S., Taupier-Letage, I., Tintore, J., Uijlenhoet, R., Wernli, H., 2014. Hymex: A 10-year multidisciplinary program on the mediterranean water cycle. Bulletin of the American Meteorological Society 95, 1063–1082. doi:10.1175/BAMS-D-12-00242.1.

Ducrocq, V., Braud, I., Davolio, S., Ferretti, R., Flamant, C., Jansa, A., Kalthoff, N., Richard, E., Taupier-Letage, I., Ayral, P.A., Belamari, S., Berne, A., Borga, M., Boudevillain, B., Bock, O., Boichard, J.L., Bouin, M.N., Bousquet, O., Bouvier, C., Chiggiato, J., Cimini, D., Corsmeier, U., Coppola, L., Cocquerez, P., Defer, E., Delanoë, J., Girolamo, P.D., Doerenbecher, A.,

Drobinski, P., Dufournet, Y., Fourrié, N., Gourley, J.J., Labatut, L., Lambert, D., Coz, J.L., Marzano, F.S., Molinié, G., Montani, A., Nord, G., Nuret, M., Ramage, K., Rison, W., Roussot, O., Said, F., Schwarzenboeck, A., Testor, P., Baelen, J.V., Vincendon, B., Aran, M., Tamayo, J., 2014. Hymex-sop1: The field campaign dedicated to heavy precipitation and flash flooding in the northwestern mediterranean. Bulletin of the American Meteorological Society 95, 1083–1100. doi:10.1175/BAMS-D-12-00244.1.

Evin, G., Blanchet, J., Paquet, E., Garavaglia, F., Penot, D., 2016. A regional model for extreme rainfall based on weather patterns subsampling. Journal of Hydrology 541, Part B, 1185 – 1198. doi:http://dx.doi.org/10.1016/j.jhydrol.2016.08.024.

Evin, G., Favre, A.C., Hingray, B., 2018. Stochastic generation of multi-site daily precipitation focusing on extreme events. Hydrology and Earth System Sciences 22, 655–672. doi:10.5194/hess-22-655-2018.

Favre, A.C., Quessy, J.F., Toupin, M.H., 2018. The new family of fisher copulas to model upper tail dependence and radial asymmetry: Properties and application to high-dimensional rainfall data. Environmetrics 29, e2494. doi:10.1002/env.2494.

Garavaglia, F., Gailhard, J., Paquet, E., Lang, M., Garçon, R., Bernardara, P., 2010. Introducing a rainfall compound distribution model based on weather patterns sub-sampling. Hydrology and Earth System Sciences 14, 951–964. doi:10.5194/hess-14-951-2010.

Garavaglia, F., Lang, M., Paquet, E., Gailhard, J., Garçon, R., Renard, B., 2011. Reliability and robustness of rainfall compound distribution model based on weather pattern sub-sampling. Hydrology and Earth System Sciences 15, 519–532. doi:10.5194/hess-15-519-2011.

Grouillet, B., Ruelland, D., Vaittinada Ayar, P., Vrac, M., 2016. Sensitivity analysis of runoff modeling to statistical downscaling models in the western

mediterranean. Hydrology and Earth System Sciences 20, 1031–1047. doi:10.5194/hess-20-1031-2016.

Guillot, G., 1999. Approximation of sahelian rainfall fields with meta-gaussian random functions. Stochastic Environmental Research and Risk Assessment 13, 100–112. doi:10.1007/s004770050034.

Guillot, G., Lebel, T., 1999. Approximation of sahelian rainfall fields with meta-gaussian random functions. Stochastic Environmental Research and Risk Assessment 13, 113–130. doi:10.1007/s004770050035.

Gutiérrez, J.M., D., M., M., W., R., H., E., H., R., B., O., R., J., W., R., W., S., K., D., S.M., S., H., J., B., A., C., R., M., M., I., M., V., M., D., J., R., J., P., O., R., J., R., B., H., D., R., J., C.M., P., R., T., Z., M., T., T., B., P., Š., J., B., R., P., E., K.D., M., F.A., M., C.R., M., S.P.M., B., C., C., P., 2018. An intercomparison of a large ensemble of statistical downscaling methods over europe: Results from the value perfect predictor cross-validation experiment. International Journal of Climatology doi:10.1002/joc.5462.

Hughes, J.P., Guttorp, P., 1994. Incorporating spatial dependence and atmospheric data in a model of precipitation. Journal of Applied Meteorology 33, 1503–1515. doi:0.1175/1520-0450(1994)033<1503:ISDAAD>2.0.CO;2.

Jha, S.K., Mariethoz, G., Evans, J., McCabe, M.F., Sharma, A., 2015. A space and time scale-dependent nonlinear geostatistical approach for downscaling daily precipitation and temperature. Water Resources Research 51, 6244–6261. doi:10.1002/2014WR016729.

Joe, H., 2014. Dependence Modeling with Copulas. Chapman & Hall/CRC Monographs on Statistics & Applied Probability, Taylor & Francis.

Kendall, M., Stuart, A., Ord, J., 1979. Inference and relationship, volume 2 of the advanced theory of statistics. Charles Grifin and Co Ltd 4.

Kleiber, W., Katz, R.W., Rajagopalan, B., 2012. Daily spatiotemporal precipitation simulation using latent and transformed gaussian processes. Water Resources Research 48. doi:10.1029/2011WR011105. w01523.

Leander, R., Buishand, T.A., 2009. A daily weather generator based on a two-stage resampling algorithm. Journal of Hydrology 374, 185 – 195. doi:https://doi.org/10.1016/j.jhydrol.2009.06.010.

Leblois, E., Creutin, J.D., 2013. Space-time simulation of intermittent rainfall with prescribed advection field: Adaptation of the turning band method. Water Resources Research 49, 3375–3387. doi:10.1002/wrcr.20190.

Leonard, M., Lambert, M.F., Metcalfe, A.V., Cowpertwait, P.S.P., 2008. A space-time neyman–scott rainfall model with defined storm extent. Water Resources Research 44. doi:10.1029/2007WR006110.

Li, S.T., Hammond, J.L., 1975. Generation of pseudorandom numbers with specified univariate distributions and correlation coefficients. IEEE Transactions on Systems, Man, and Cybernetics , 557–561.

Matheron, G., 1989. The internal consistency of models in geostatistics, in: Armstrong, M. (Ed.), Geostatistics. Springer Netherlands. volume 4 of *Quantitative Geology and Geostatistics*, pp. 21–38. URL: http://dx.doi.org/10.1007/978-94-015-6844-9_2, doi:10.1007/978-94-015-6844-9_2.

Mehrotra, R., Sharma, A., 2007. A semi-parametric model for stochastic generation of multi-site daily rainfall exhibiting low-frequency variability. Journal of Hydrology 335, 180 – 193. doi:https://doi.org/10.1016/j.jhydrol.2006.11.011.

Nelsen, R., 2007. An Introduction to Copulas. Springer Series in Statistics, Springer New York.

Nuissier, O., Ducrocq, V., Ricard, D., Lebeaupin, C., Anquetin, S., 2008. A numerical study of three catastrophic precipitating events over southern france.

i: Numerical framework and synoptic ingredients. Quarterly Journal of the Royal Meteorological Society 134, 111–130. doi:10.1002/qj.200.

Onof, C., Chandler, R.E., Kakou, A., Northrop, P., Wheater, H.S., Isham, V., 2000. Rainfall modelling using poisson-cluster processes: a review of developments. Stochastic Environmental Research and Risk Assessment 14, 384–411. doi:10.1007/s004770000043.

Paciorek, C.J., Schervish, M.J., 2006. Spatial modelling using a new class of nonstationary covariance functions. Environmetrics 17, 483–506. doi:10.1002/env.785.

Papalexiou, S.M., 2018. Unified theory for stochastic modelling of hydroclimatic processes: Preserving marginal distributions, correlation structures, and intermittency. Advances in Water Resources 115, 234 – 252. doi:https://doi.org/10.1016/j.advwatres.2018.02.013.

Paquet, E., Garavaglia, F., Garçon, R., Gailhard, J., 2013. The schadex method: A semi-continuous rainfall–runoff simulation for extreme flood estimation. Journal of Hydrology 495, 23 – 37. doi:10.1016/j.jhydrol.2013.04.045.

Paschalis, A., Molnar, P., Fatichi, S., Burlando, P., 2013. A stochastic model for high-resolution space-time precipitation simulation. Water Resources Research 49, 8400–8417. doi:10.1002/2013WR014437.

Peleg, N., Fatichi, S., Paschalis, A., Molnar, P., Burlando, P., 2017. An advanced stochastic weather generator for simulating 2-d high-resolution climate variables. Journal of Advances in Modeling Earth Systems 9, 1595–1627. doi:10.1002/2016MS000854.

Peleg, N., Morin, E., 2014. Stochastic convective rain-field simulation using a high-resolution synoptically conditioned weather generator (hires-wg). Water Resources Research 50, 2124–2139. doi:10.1002/2013WR014836.

Pesonen, M., Pesonen, H., Nevalainen, J., 2015. Covariance matrix estimation for left-censored data. Computational Statistics & Data Analysis 92, 13 – 25. doi:http://dx.doi.org/10.1016/j.csda.2015.06.005.

Quessy, J.F., Rivest, L.P., Toupin, M.H., 2016. On the family of multivariate chi-square copulas. Journal of Multivariate Analysis 152, 40 – 60. doi:https://doi.org/10.1016/j.jmva.2016.07.007.

Rasmussen, P.F., 2013. Multisite precipitation generation using a latent autoregressive model. Water Resources Research 49, 1845–1857. doi:10.1002/wrcr.20164.

Risser, M.D., 2015. Spatially-varying covariance functions for nonstationary spatial process modeling. Electronic Thesis or Dissertation. Ohio State University URL: http://rave.ohiolink.edu/etdc/view?acc_num=osu1437409380.

Schaefer, M.G., Barker, B.L., 2002. Stochastic event flood model. Mathematical models of small watershed hydrology and applications , 707–748.

Serinaldi, F., Kilsby, C.G., 2014. Simulating daily rainfall fields over large areas for collective risk estimation. Journal of Hydrology 512, 285 – 302. doi:http://dx.doi.org/10.1016/j.jhydrol.2014.02.043.

Sigrist, F., Künsch, H.R., Stahel, W.A., 2012. A dynamic nonstationary spatio-temporal model for short term prediction of precipitation. Ann. Appl. Stat. 6, 1452–1477. doi:10.1214/12-AOAS564.

Sparks, N.J., Hardwick, S.R., Schmid, M., Toumi, R., 2018. Image: a multivariate multi-site stochastic weather generator for european weather and climate. Stochastic Environmental Research and Risk Assessment 32, 771–784. doi:10.1007/s00477-017-1433-9.

Steinschneider, S., Brown, C., 2013. A semiparametric multivariate, multisite weather generator with low-frequency variability for use in climate risk assessments. Water Resources Research 49, 7205–7220. doi:10.1002/wrcr.20528.

Thompson, C.S., Thomson, P.J., Zheng, X., 2007. Fitting a multisite daily rainfall model to new zealand data. Journal of Hydrology 340, 25 – 39. doi:https://doi.org/10.1016/j.jhydrol.2007.03.020.

Vaittinada Ayar, P., Vrac, M., Bastin, S., Carreau, J., Déqué, M., Gallardo, C., 2016. Intercomparison of statistical and dynamical downscaling models under the euro- and med-cordex initiative framework: present climate evaluations. Climate Dynamics 46, 1301–1329. URL: http://dx.doi.org/10.1007/s00382-015-2647-5, doi:10.1007/s00382-015-2647-5.

Verdin, A., Rajagopalan, B., Kleiber, W., Katz, R.W., 2015. Coupled stochastic weather generation using spatial and generalized linear models. Stochastic Environmental Research and Risk Assessment 29, 347–356. doi:10.1007/s00477-014-0911-6.

Vischel, T., Lebel, T., Massuel, S., Cappelaere, B., 2009. Conditional simulation schemes of rain fields and their application to rainfall–runoff modeling studies in the Sahel. Journal of Hydrology 375, 273 – 286. doi:http://dx.doi.org/10.1016/j.jhydrol.2009.02.028. surface processes and water cycle in West Africa, studied from the AMMA-CATCH observing system.

Vrac, M., Stein, M.L., Hayhoe, K., 2007. Statistical downscaling of precipitation through nonhomogeneous stochastic weather typing. Climate Research 34, 169–184. doi:10.3354/cr00696.

Wilks, D., 1998. Multisite generalization of a daily stochastic precipitation generation model. Journal of Hydrology 210, 178 – 191. doi:http://dx.doi.org/10.1016/S0022-1694(98)00186-3.

Wilks, D.S., 2010. Use of stochastic weathergenerators for precipitation downscaling. Wiley Interdisciplinary Reviews: Climate Change 1, 898–907. doi:10.1002/wcc.85.

Wilks, D.S., 2012. Stochastic weather generators for climate-change downscaling, part ii: multivariable and spatially coherent multisite downscaling. Wiley

Interdisciplinary Reviews: Climate Change 3, 267–278. doi:10.1002/wcc.167.

Wilks, D.S., Wilby, R.L., 1999. The weather generation game: a review of stochastic weather models. Progress in Physical Geography 23, 329–357. doi:10.1177/030913339902300302.

Yang, C., Chandler, R.E., Isham, V.S., Wheater, H.S., 2005. Spatial-temporal rainfall simulation using generalized linear models. Water Resources Research 41, W11415. doi:10.1029/2004WR003739.

Yiou, P., 2014. AnaWEGE: a weather generator based on analogues of atmospheric circulation. Geoscientific Model Development 7, 531–543. doi:10.5194/gmd-7-531-2014.

Zucchini, W., Guttorp, P., 1991. A hidden markov model for space-time precipitation. Water Resources Research 27, 1917–1923. doi:10.1029/91WR01403.